Monthly Notices of the ROYAL ASTRONOMICAL SOCIETY

MNRAS **438,** 278–306 (2014) doi:10.1093/mnras/stt2176
Advance Access publication 2013 December 21

Three-dimensional magnetohydrodynamic simulations of the Crab nebula

Oliver Porth,[1,2]★ Serguei S. Komissarov[1]★ and Rony Keppens[2]

[1]*Department of Applied Mathematics, The University of Leeds, Leeds LS2 9GT, UK*
[2]*Centre for mathematical Plasma Astrophysics, Department of Mathematics, KU Leuven, Celestijnenlaan 200B, B-3001 Leuven, Belgium*

Accepted 2013 November 7. Received 2013 November 7; in original form 2013 August 9

ABSTRACT

In this paper, we give a detailed account of the first three-dimensional (3D) relativistic magnetohydrodynamic simulations of pulsar wind nebulae, with parameters most suitable for the Crab nebula. In contrast to the previous 2D simulations, we also consider pulsar winds with much stronger magnetization, up to $\sigma \simeq$ few. The 3D models preserve the separation of the post-termination shock flow into the equatorial and polar components, but the polar jets are disrupted by the kink mode of the current driven instability and 'dissolve' into the main body of the nebula after propagation of several shock radii. With the exception of the region near the termination shock, the 3D models do not exhibit the strong z-pinch configuration characteristic of the 1D and 2D models. Contrary to the expectations based on 1D analytical and semi-analytical models, the 3D solutions with highly magnetized pulsar winds still produce termination shocks with radii comparable to those deduced from the observations. The reason for this is not only the randomization of magnetic field observed in the 3D solutions, but also the magnetic dissipation inside the nebula. Assuming that the particle acceleration occurs only at the termination shock, we produced synthetic maps of the Crab nebula synchrotron emission. These maps retain most of the features revealed in the previous 2D simulations, including thin wisps and the inner knot. The polarization and variability of the inner knot is in a particularly good agreement with the observations of the Crab nebula and the overall polarization of the inner nebula is also reproduced quite well. However, the polar jet is not as bright as observed, suggesting that an additional particle acceleration, presumably related to the magnetic dissipation, has to be invoked.

Key words: instabilities – MHD – relativistic processes – shock waves – pulsars: individual: Crab – ISM: supernova remnants.

1 INTRODUCTION

The Crab nebula is one of the most iconic cosmic objects at present time. The history of astronomical and astrophysical studies related to the 'Crab' is long and eventful, with the discovery of the Crab pulsar and its connection to the 'guest star', observed by Chinese and Arab astronomers in the year 1054, being the most commented on highlights. The more recent discoveries include the dynamic jet and torus around the Crab pulsar and the still mysterious gamma-ray flares. At the time of writing this manuscript, SAO/NASA ADS search engine returns 1598 hits for papers with words 'crab' and 'nebula' in their titles and 4358 hits for papers with these words in their abstracts.

The main interest to the Crab nebula in modern astrophysics stems from the fact that it is one of the brightest sources of non-thermal emission in the sky throughout the whole observational range of photon energies. This emission comes from the ultrarelativistic plasma filling the interior of the nebula. The relatively small overall linear size of the nebula, which is only several light years across, allows direct observations of the global dynamics of this plasma, whereas its large angular size (of 7 arcmin) ensures that its spatial structure is well resolved, allowing studies of small-scale structural variability. There are other types of objects in the Universe which share many similarities with the Crab nebula, e.g. radio galaxies, quasars, gamma-ray bursters, which are of great interest to researchers of various specializations. They all provide important clues to the properties of relativistic plasma. Yet given its unique parameters, the Crab nebula remains the most productive testbed of modern high-energy astrophysics.

The observational data, accumulated over many years, make a compelling case for the relativistic plasma being continuously supplied into the nebula by the Crab pulsar; in the form of an ultrarelativistic magnetized wind (Rees & Gunn 1974; Kennel & Coroniti 1984a). The early quantitative models of the interaction between this wind and the much slower massive supernova shell were developed

★ E-mail: o.porth@leeds.ac.uk (OP); serguei@maths.leeds.ac.uk (SSK)

© 2013 The Authors
Published by Oxford University Press on behalf of the Royal Astronomical Society

Downloaded from http://mnras.oxfordjournals.org/ at University of Leeds on April 1, 2016

within the framework of ideal relativistic magnetohydrodynamics (RMHD), using one-dimensional (1D) approximations. They fitted the observational parameters of the nebula and its pulsar quite well, but required the Poynting flux of the pulsar wind to be only a small fraction, $\sim 10^{-3}$, of the total wind power (Rees & Gunn 1974; Kennel & Coroniti 1984a; Emmering & Chevalier 1987; Begelman & Li 1992). Assuming that the electrons producing the observed non-thermal synchrotron component of the nebula emission were accelerated at the termination shock of the wind, these models could explain its spectrum from the optical to gamma-ray energies (Kennel & Coroniti 1984b). The even more energetic inverse-Compton emission, which was discovered much later, also fits within this scenario very well (Atoyan & Aharonian 1996; Meyer, Horns & Zechlin 2010).

Some shortcomings of the 1D model were obvious from the start. For example, the nebula is not spherical but shows significant elongation, and it is filled with a complex network of line-emitting filaments. However, these were ignored until the X-ray *Chandra* observations revealed the spectacular axisymmetric 'torus' in the inner Crab nebula as well as a weak jet apparently originated from the pulsar (Weisskopf et al. 2000). This discovery prompted a revision of the 1D model by taking into account the earlier theoretical studies of magnetically dominated pulsar winds which concluded that they must be highly aspherical, with the wind power scaling as $\sin^2\theta$, where θ is the angle measured from the rotational axis of the pulsar (Michel 1973; Bogovalov 1999). Recent 3D RMHD simulations of pulsar winds show a somewhat different θ dependence, but generally confirm the theory (Tchekhovskoy, Spitkovsky & Li 2012). This implies that the wind termination shock must be flattened at the poles, and that the freshly supplied plasma enters the nebula predominantly as an equatorial flow, providing a nice explanation of the Crab's torus (Bogovalov & Khangoulian 2002; Lyubarsky 2002). The nature of its jet is less obvious and remained controversial for a while. In particular, Lyubarsky (2002) proposed that the jet is formed downstream of the termination because of the strong hoop stress of the azimuthal magnetic field supplied by the wind, which pulls the shocked plasma towards the wind symmetry axis and then squeezes it away along the axis, very much like toothpaste is extracted from its container.

In order to check these ideas and study the 2D models in detail, a number of groups carried out axisymmetric RMHD simulations of pulsar wind nebulae (PWNe; Komissarov & Lyubarsky 2003, 2004; Del Zanna, Amato & Bucciantini 2004; Bogovalov et al. 2005). Although they employed rather different computer codes, all these simulations produced quite similar results. For the pulsar wind parameters similar to those of the 1D model of Kennel & Coroniti (1984a), the numerical solutions could reproduce the observed jet–torus structure of the Crab nebula. In addition, even the rather crude initial attempts to model the PWN synchrotron emission using such numerical solutions provided a neat explanation for the most compact and bright feature of the nebula, its mysterious *Hubble Space Telescope* (*HST*) knot 1, which is located within 1 arcsec from the Crab pulsar (Hester et al. 1995). In these models, the knot is a Doppler-beamed emission from the patch of the highly oblique termination shock where the post-shock flow is still highly relativistic and directed towards the observer (Komissarov & Lyubarsky 2004). Later, the more advanced models, following the approach of Kennel & Coroniti (1984b), confirmed that this feature was robust (Del Zanna et al. 2006; Komissarov & Lyutikov 2011). They also demonstrated that the models could explain the observed spectrum and polarization of the Crab nebula (Bucciantini et al. 2005; Volpi et al. 2008).

These early numerical simulations had rather low resolution and hence high numerical viscosity, damping short length-scale motions in the nebula. Moreover, they also imposed equatorial symmetry and studied the flow only in one hemisphere. When these limitations were eased in the later study by Camus et al. (2009), a much more dynamic and unsteady flow structure emerged. The main new feature was the highly distorted termination shock, variable on the scale comparable to its light crossing time and the highly inhomogeneous flow entering the nebula. While the overall jet–torus structure still persisted, the synthetic synchrotron images of the nebula also included bright fine filaments moving away from the pulsar with the initial speed approaching a large fraction of the speed of light. These are highly reminiscent of the so-called wisps of Crab nebula, which were discovered almost a century ago by Lampland (1921), who also reported their variability. This variability was carefully studied by Scargle (1969), who concluded that it is likely related to the fast motion of the wisps. However, only much more recent observations were able to deliver a firm evidence in favour of this interpretation (Hester et al. 2002).

In spite of all these successes of the magnetohydrodynamic (MHD) models, one issue, the so-called σ problem, has been overshadowing them almost from the start. They all utilized the pulsar wind models, where the ratio of the Poynting flux to the kinetic energy flux, the parameter traditionally denoted as σ, was much less than unity. In fact, the 1D model would fit the observations only for $\sigma \sim 10^{-3}$. Moreover, for significantly higher values of σ, the MHD solution could not be found, with the termination shock collapsing on to the wind origin (Kennel & Coroniti 1984a). In contrast, the theory of pulsar magnetospheres predicts winds which are strongly Poynting dominated, at least at their base (see Arons 2012, and references therein).

Several possible explanations of this σ problem have been put forward over the years. The simplest one is that the electromagnetic energy of the pulsar wind is converted into kinetic energy of the wind on its way from the pulsar to the termination shock. Although claims have been made that ideal MHD acceleration mechanisms can provide the required energy conversion (e.g. Vlahakis 2004), it has now become clear that this is not the case (e.g. Komissarov et al. 2009; Lyubarsky 2009, 2010).

The acceleration can be facilitated via non-ideal processes, involving magnetic dissipation. This is only relevant in the so-called striped-wind zone of pulsar winds where alternations of the magnetic field direction are expected on the length-scale of the light cylinder radius (Coroniti 1990). For the wind of the Crab pulsar, the dissipation length-scale still significantly exceeds the radius of the wind termination shock (Lyubarsky & Kirk 2001), unless the pulsar produces much more plasma compared to the predictions of the current models of pair production in pulsar magnetospheres (see Arons 2012, and references therein). Alternatively, the energy associated with the alternating component of magnetic field of the striped wind can be rapidly dissipated at the termination shock itself (e.g. Lyubarsky 2003; Sironi & Spitkovsky 2011b; Amano & Kirk 2013). Although the striped-wind model allows conversion of a large fraction of the total Poynting flux into the internal energy of PWN plasma, much more is needed to approach the target value of $\sigma \sim 10^{-3} \div 10^{-2}$. Indeed, the dissipation is confined to the striped zone of the wind and only the alternating component of magnetic field dissipates. Closer to the poles, the magnetization of the pulsar wind plasma remains very high even after it crosses the termination shock, and as a result, the overall magnetization of the plasma injected into the nebula is much higher than that of the Kennel–Coroniti model, unless the striped zone spreads over almost the

Downloaded from http://mnras.oxfordjournals.org/ at University of Leeds on April 1, 2016

entire wind, implying that the pulsar is an almost orthogonal rotator (Coroniti 1990; Komissarov 2013).

In contrast to these ideas, Begelman (1998) argues that the axisymmetric models may be highly unrealistic when it comes to the global structure of PWN. He has shown that the plasma configuration assumed in these models is unstable to the magnetic kink instability and speculated that the disrupted configuration may be less demanding on the magnetization of pulsar winds. Indeed, one would expect the magnetic pressure due to randomized magnetic field to dominate the mean Maxwell stress tensor, and the adiabatic compression to have the same effect on the magnetic pressure as on the thermodynamic pressure of relativistic gas. Under such conditions, the global dynamics of PWN produced by high-σ winds may not be that much different from those of PWN produced by particle-dominated winds. These expectations have received strong support from the recent numerical studies (Mizuno et al. 2011) of the magnetic kink instability for the cylindrical magnetostatic configuration, which was used in Begelman & Li (1992) to model PWN. These simulations have shown a relaxation towards a quasi-uniform total pressure distribution inside the computational domain on the dynamical time-scale. Although important, these simulations do not claim to model PWN, simply because the continuous injection of magnetic flux and energy into PWN by their pulsar winds is not accounted for.

In addition to the dissipation of magnetic stripes in the wind or at the termination shock, the magnetic dissipation could occur inside PWN as well (Lyutikov 2010; Komissarov 2013). In fact, the development of the kink instability is bound to facilitate such dissipation, as this has already been demonstrated in the simulations by Mizuno et al. (2011). In principle, simultaneous observations of both the synchrotron and inverse-Compton emission allow us to measure the energy distribution between the magnetic fields and the emitting electrons (and positrons). From a simple 'one-zone' model of the Crab nebula, it follows that its magnetic energy is only a small fraction, $\sim 1/30$, of the energy stored in the emitting particles (Meyer et al. 2010; Komissarov 2013). This shows that unless the striped-wind zone of the Crab's wind fills almost the entire wind volume, there must be a substantial magnetic dissipation inside the nebula (Komissarov 2013). This is certainly the case for the magnetic inclination angle of the Crab pulsar $\alpha \sim 45^\circ$, found by Harding et al. (2008) in their modelling of the high-energy emission of the pulsar.

The issue of magnetic dissipation is now gradually moving into the focus of high-energy astrophysics. For a long time, it was widely accepted that the ultrarelativistic particles producing the observed non-thermal emission in all astrophysical phenomena are mainly accelerated at shocks. However, this is very problematic in the case of highly magnetized flows, which are often invoked in theories of relativistic galactic and extragalactic jets and gamma-ray bursts (GRBs). First, even strong, high Mach number shocks, in high-σ plasma are much less dissipative compared to their low-σ counterparts (e.g. Kennel & Coroniti 1984a; Komissarov 2012). But what is even more important is that the recent advanced particle-in-cell (PIC) simulations show that the acceleration of non-thermal particles does not operate at such shocks (Sironi & Spitkovsky 2009, 2011a). Although the ideal MHD conversion of magnetic energy into the bulk motion energy of particles is less of an issue for collimated jets than for uncollimated pulsar winds (e.g. Vlahakis & Königl 2004; Komissarov et al. 2007; Lyubarsky 2009; Tchekhovskoy, Narayan & McKinney 2010), it is still quite impossible to reach $\sigma < 10^{-2}$, required by the PIC simulations in order to allow the particle acceleration. This is why the magnetic reconnection sites are now considered as more promising candidates for the particle acceleration.

The recently discovered short intense gamma-ray flares in the Crab nebula (Abdo et al. 2011; Tavani et al. 2011) seem to be the first clear signatures of magnetic reconnection in relativistic plasma. The very high photon energies of the flares, exceeding 100 MeV, require strong Doppler boosting in order to overcome the radiation reaction limit of shock acceleration. However during the flares, none of the bright and compact, and hence presumably Doppler-boosted, emission features in the nebula show increased activity during the flares at lower energies – in conflict with what is expected in the case of shock acceleration mechanisms (Weisskopf 2013). In contrast, the electrostatic acceleration in reconnection current sheets readily produces a quasi-monoenergetic spectrum of particle energies (Cerutti, Uzdensky & Begelman 2012; Clausen-Brown & Lyutikov 2012).

In this paper, we provide a detailed account of the first 3D RMHD simulations of the Crab nebula. Our main motivation was to study the effects which the additional degree of freedom has on the structure and dynamics of PWN. Mainly, we wanted to see (i) if the magnetic field would become randomized just enough to resolve the σ problem and yet to agree with the high polarization typical for the inner Crab nebula (Hickson & van den Bergh 1990; Moran et al. 2013), (ii) if the jet–torus structure, especially its jet component, will be preserved and (iii) whether the strong non-stationary dynamics of the termination shock discovered in 2D simulations and connected to the wisp production will carry on in 3D. Preliminary results of the simulations have been reported in Porth, Komissarov & Keppens (2013).

2 SIMULATIONS OVERVIEW

2.1 Equations and numerical method

We solve the equations of ideal RMHD in Minkowski space–time. These are the continuity equation

$$\frac{\partial}{\partial t}(\rho\Gamma) + \nabla_i(\rho\Gamma v^i) = 0, \tag{1}$$

the energy equation

$$\frac{\partial}{\partial t}\left(w\Gamma^2 - P + \frac{B^2+E^2}{8\pi}\right) + \nabla_i(w\Gamma^2 v^i + S^i) = 0, \tag{2}$$

the momentum equations

$$\frac{\partial}{\partial t}\left(w\Gamma^2 v^j + \frac{S^j}{c^2}\right) + \nabla_i(w\Gamma^2 v^i v^j + P g^{ij} + T^{ij}) = 0 \tag{3}$$

and the Faraday equation

$$\frac{1}{c}\frac{\partial}{\partial t}B^j + \mathrm{e}^{jik}\frac{\partial}{\partial x^i}E_k = 0, \tag{4}$$

where ρ and P are the rest mass density and thermodynamic pressure, respectively, $w = \rho c^2 + \gamma P/(\gamma - 1)$ is the relativistic enthalpy, γ is the adiabatic index ($\gamma = 4/3$ in the simulations), v and Γ are its velocity and Lorentz factor, B and E are the magnetic and electric fields, $S^i = e^{ijk}E_j B_k/4\pi c$ is the Poynting vector, g^{ij}, e^{ijk} and ∇_i are the metric tensor, the Levi-Civita tensor and the covariant derivative operator of Euclidean space, respectively, $T^{ij} = -E^iE^j - B^iB^j + (B^2+E^2)g^{ij}/2$ is the Maxwell stress tensor. These equations are supplemented with the Ohm's law of ideal MHD,

$$E^i = -\frac{1}{c}e^{ijk}v_j B_k. \tag{5}$$

Downloaded from http://mnras.oxfordjournals.org/ at University of Leeds on April 1, 2016

The numerical simulations are performed with MPI-AMRVAC (Keppens et al. 2012), which integrates the special RMHD conservation laws using finite volume discretization and adaptive mesh refinement (AMR). In our simulations, we use the following hybrid approach. Outside of the termination shock, we apply the compact stencil third-order reconstruction scheme (LIM03; Čada & Torrilhon 2009), combined with an HLLC Riemann solver (Honkkila & Janhunen 2007). In the pulsar wind and around the termination shock, we utilize a robust total variation diminishing Lax–Friedrich scheme in combination with the minmod limiter. The solution is advanced in time with a third-order Runge–Kutta integration. The divergence-free condition for $\boldsymbol{B}$ is enforced using the Powell (1994) source term approach.

Our 3D simulations are performed in the Cartesian coordinates. We employ a cubic domain with the edge length of 2×10^{19} cm, large enough to contain today's Crab nebula. The large box size also ensures that no backreaction from the outflow boundaries can influence the simulated nebula bubble. The base level of AMR includes 64^3 cells. Four more levels are used to resolve the expanding nebula bubble, with the cell size of $\Delta x = 1.95 \times 10^{16}$ cm at the fifth level. Higher resolution cases are achieved by increasing this nebula refinement up to the ninth level.

A higher resolution is required to properly resolve the termination shock and the flow near the origin. To this end, additional grid levels centred on the termination shock are automatically activated, the actual number being dependent on the shock size. For the simulations presented in this paper, normally 3 to 4 extra grid levels are employed, resulting in 8 to 9 levels in total. Up to 20 grid levels in total are allowed in the vicinity of the origin and in order to speed up the simulations, grid blocks that only hold the stationary wind solution are normally de-activated from further temporal updates and automatically re-activated when the termination shock comes within their range.

In order to study the impact of the axisymmetry condition, we also performed 2D simulations whose numerical setup was identical to that of corresponding 3D simulations in all respects, with the exception of cylindrical coordinates $\{r, z\}$. The standard reflective boundary conditions were applied at the symmetry axis $r = 0$.

2.2 Problem initialization

Initially, the computational domain is split in two zones separated by a spherical boundary of radius $r_i = 10^{18}$ cm. The outer zone describes a radially expanding cold supernova shell. The solution in this zone has Hubble's velocity profile

$$v = v_{\rm i}\left(\frac{r}{r_{\rm i}}\right) \tag{6}$$

and constant density $\rho_{\rm e}$. The values of parameters $\rho_{\rm e}$ and $v_{\rm i}$ are determined from the mass and energy of the shell as follows.

Assuming that the ejecta of total mass M_e is distributed in a shell of constant density ρ_e between radii r_i and r_e, we have

$$\rho_e = \frac{M_e}{\int_{r_i}^{r_e} 4\pi r^2 {\rm d}r}. \tag{7}$$

The velocity at the outer edge of the shell v_e can be found as

$$v_e = \left[\frac{E_e}{\int_{r_i}^{r_e} 2\pi r^4/r_e^2 \rho_e {\rm d}r}\right]^{1/2} = \left(\frac{10}{3}\frac{E_e}{M_e}\right)^{1/2} r_e \left(\frac{r_e^3 - r_i^3}{r_e^5 - r_i^5}\right)^{1/2}, \tag{8}$$

where E_e is the total kinetic energy of the shell. In a self-similar evolution, the ratio of inner to outer shell radius $x \equiv r_i/r_e$ remains constant during the entire expansion. This allows us to eliminate r_i and obtain

$$v_e = \left(\frac{10}{3}\frac{E_e}{M_e}\right)^{1/2} \left(\frac{1-x^3}{1-x^5}\right)^{1/2}, \tag{9}$$

which depends only mildly on x when $x \ll 1$. For example, for $x = 1/5$, the x-dependent factor of relation (9) is $\simeq 0.996$ and hence this dependence is dropped in the following, to give

$$v_e = \left(\frac{10}{3}\frac{E_e}{M_e}\right)^{1/2}. \tag{10}$$

The velocity v_i of the initial expansion at the contact discontinuity is simply $v_i = x v_e$. For our simulations, we adopt the parameters $M_e = 3\,{\rm M}_\odot = 6 \times 10^{33}$ g and $E_e = 10^{51}$ erg in accordance with Del Zanna et al. (2004). We choose $x = 1/5$ to obtain $v_i = 1495\,{\rm km\,s^{-1}}$. Since we do not study the dynamics at the forward supernova blast in this work, the outer radius r_e has no further significance and we simply continue this supernova remnant (SNR) solution up to the outer boundary of the computational domain.

The inner zone is initially filled with unshocked pulsar wind. In our model of the wind, we assume that the alternating component of magnetic field in its striped zone has completely dissipated along the way from the pulsar to the PWN. Although this may not be the case and most of the dissipation occurs instead at the termination shock, dynamically this makes no difference (Lyubarsky 2003). The total energy flux density of the wind follows that of the monopole model (Michel 1973)

$$f_{\rm tot}(r,\theta) = \frac{L}{L'}\left(\frac{1}{r^2}\right)\left(\sin^2\theta + b\right). \tag{11}$$

The parameter $b = 0.03$ is added for numerical reasons to avoid vanishing energy flux at the poles. $L' = \pi(8/3 + 4b)$ simply gives the normalization such that the total power in the pulsar wind corresponds to the current spin-down luminosity of the Crab pulsar, $L = 5 \times 10^{38}\,{\rm erg\,s^{-1}}$ (e.g. Hester 2008, and references therein). This energy is divided between the magnetic, $f_{\rm m}$, and kinetic, $f_{\rm k}$, terms

$$f_{\rm m}(r,\theta) = \sigma(\theta)\frac{f_{\rm tot}(\theta,r)}{1+\sigma(\theta)}, \quad f_{\rm k}(r,\theta) = \frac{f_{\rm tot}(r,\theta)}{1+\sigma(\theta)}, \tag{12}$$

where $\sigma(\theta)$ is the latitude-dependent wind magnetization.

For simplicity, we assume that before reaching the dissipation zone of magnetic stripes, the wind magnetization saturates at

$$\tilde{\sigma}_0(\theta) = \begin{cases} (\theta/\theta_0)^2\ \sigma_0; & \theta \le \theta_0 \\ \sigma_0; & \theta > \theta_0, \end{cases} \tag{13}$$

where the additional (small) parameter $\theta_0 = 10^\circ$ was introduced to ensure that the Poynting flux vanishes on the symmetry axis (σ_0 is one of the model parameters reported in Table 1). The dissipation of magnetic stripes changes the magnetization of the striped-wind zone so that

$$\sigma(\theta) = \frac{\tilde{\sigma}_0(\theta)\chi_\alpha(\theta)}{1+\tilde{\sigma}_0(\theta)(1-\chi_\alpha(\theta))}, \tag{14}$$

where

$$\chi_\alpha(\theta) = \begin{cases} (2\phi_\alpha(\theta)/\pi - 1)^2, & \pi/2 - \alpha < \theta < \pi/2 + \alpha \\ 1, & \text{otherwise} \end{cases}, \tag{15}$$

with $\phi_\alpha(\theta) \equiv \arccos(-\cot(\theta)\cot(\alpha))$. Here, α is the magnetic inclination angle of the pulsar, which determines the size of the striped-wind zone (Komissarov 2013). Equations (14) and (15) can be read

Downloaded from http://mnras.oxfordjournals.org/ at University of Leeds on April 1, 2016

Table 1. Overview of simulations. Designation 2D* means 2D axisymmetric simulations with enforced equatorial symmetry, where only the Northern hemisphere is simulated and the condition $[B_\phi] = 2B_\phi$ is imposed at the equator. Designation 2D** is the same as 2D* but with the boundary condition $[B_\phi] = 0$. The column labelled Δx shows the resolution in the post-shock nebula flow in the units of 10^{16} cm.

ID	α	σ_0	Dim.	Δx	$\bar{\sigma}$	$\bar{\sigma}_s$	$t_{\rm end}$
A3D	45°	0.01	3D	1.95	0.0021	0.0063	106
B3D	45°	1	3D	1.95	0.12	0.22	74
B3Dhr	45°	1	3D	0.89	0.12	0.22	54
C3D	45°	3	3D	1.95	0.19	0.31	74
D3D	10°	3	3D	1.95	1.47	2.38	54
A2D	45°	0.01	2D	1.95	0.0021	0.0063	848
B2D	45°	1	2D	1.95	0.12	0.22	800
C2D	45°	3	2D	1.95	0.19	0.31	138
D2D	10°	3	2D	1.95	1.47	2.38	63
B2Dhr	45°	1	2D	0.98	0.12	0.22	121
B2Dvhr	45°	1	2D	0.49	0.12	0.22	106
B2Duhr	45°	1	2D	0.24	0.12	0.22	74
B2Dehr	45°	1	2D	0.12	0.12	0.22	32
B2Deq	45°	1	2D*	1.95	0.12	0.22	112
B2Dhreq	45°	1	2D*	0.98	0.12	0.22	106
B2Dvhreq	45°	1	2D*	0.49	0.12	0.22	74
B2DhreqS	45°	1	2D**	0.98	0.12	0.22	106

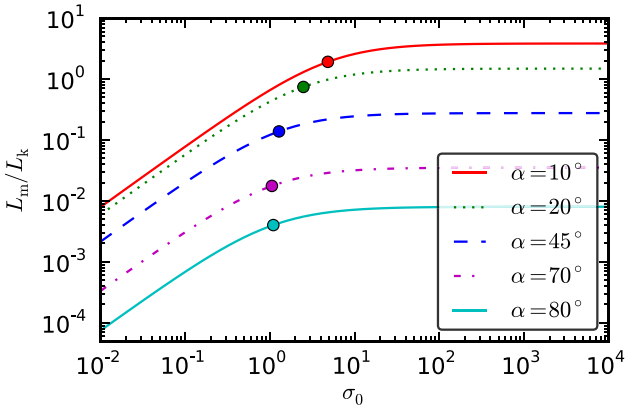

Figure 1. The ratio of electromagnetic and kinetic luminosities injected into the PWN against the magnetization parameter σ_0 of the pulsar wind for various angles of obliqueness α. The circles mark the locations where the luminosity ratio assumes half of the value corresponding to $\sigma_0 = \infty$. For $\alpha < 45°$, the saturation regime is obtained already for moderate values of $\sigma_0 \simeq 1$. This is why our dynamical simulations can provide reasonable models for the much higher magnetization, $\sigma_0 > 10^3$, predicted in the theory of pulsar magnetospheres.

as follows. For polar angles $\theta < \pi/2 - \alpha$ polarity reversals of the magnetic field are not present (unstriped region) and the initial magnetization profile $\bar{\sigma}_0(\theta)$ is obtained (with $\chi_\alpha = 1$). Starting at $\theta \geq \pi/2 - \alpha$ the striped region of the flow emerges, giving rise to a drop in $\chi_\alpha(\theta)$ and a decreasing effective magnetization that ultimately vanishes on the equator [with $\chi_\alpha(\pi/2) = 0$].

Fig. 1 shows the ratio of the wind total electromagnetic luminosity

$$L_{\rm m} = 2\pi r^2 \int_0^\pi \sin\theta \; f_{\rm m}(r,\theta)\,{\rm d}\theta \tag{16}$$

to its total kinetic luminosity

$$L_{\rm k} = 2\pi r^2 \int_0^\pi \sin\theta \; f_{\rm k}(r,\theta)\,{\rm d}\theta \tag{17}$$

as a function of σ_0 for various values of the magnetic inclination angle. In the simulations, we use $\sigma_0 = 0.01$, 1, 3 and $\alpha = 10°$, 45°. As one can see in Fig. 1, the ratio $L_{\rm m}/L_{\rm k}$ saturates for $\sigma_0 \gg 1$, with the asymptotic value being determined by the extent of the striped-wind zone. In fact, for all models, except those with very small α, this ratio is already very close to the asymptotic value when $\sigma_0 = 3$. This is why we expect our models with $\sigma_0 = 3$ not to be very different from those with much higher σ_0, which are predicted in the theory of pulsar magnetospheres. One sees that in the high-σ limit, the obliqueness α has a much larger impact on the overall wind magnetization than σ_0. Usually, the parameter α is not very well constrained observationally. However, in the case of the Crab pulsar, Harding et al. (2008) found $\alpha \simeq 45°$ by fitting the high-energy spectrum and the pulse profile. Therefore, we adopt this value for our reference case.

The magnetization of the plasma injected into the PWN is also influenced by the termination shock. As $B_\phi \beta_n = $ const. across the shock, the Poynting flux changes according to the shock compression by the factor $\eta = \beta_{n,1}/\beta_{n,2}$, where $\boldsymbol{\beta} \equiv \boldsymbol{v}/c$. For a cold, highly relativistic wind, the jump conditions for an oblique shock (see appendix of Komissarov & Lyutikov 2011) imply the compression

$$\eta(\sigma) = 6(1+\sigma)\left(1 + 2\sigma + \sqrt{1 + 16\sigma + 16\sigma^2}\right)^{-1} \tag{18}$$

and we obtain a profile for the generalized local magnetization

$$\sigma_{\rm s} \equiv \frac{f_{\rm m}}{f_{\rm tot} - f_{\rm m}} = \frac{\sigma(\theta)\eta(\sigma(\theta))}{1 + \sigma(\theta)(1 - \eta(\sigma(\theta)))}, \tag{19}$$

where the denominator includes kinetic and thermal energy. The total downstream magnetic and kinetic plus thermal luminosities, $L_{\rm m,\,s}$, $L_{\rm k\,+\,t,\,s}$, can be derived in the same way as in equations (12), (16) and (17). The effective downstream magnetization $\bar{\sigma}_s \equiv L_{\rm m,s}/L_{\rm k+t,s}$ differs from the upstream value $\bar{\sigma} \equiv L_{\rm m}/L_{\rm k}$ by a factor, which varies between one and three. For reference, the values of $\bar{\sigma}$ and $\bar{\sigma}_s$ in our simulations are listed in Table 1.

The wind's magnetic field is purely azimuthal and changes direction at the equatorial plane. Its strength, as measured in the pulsar frame, is found via

$$B_\phi(r,\theta) = \pm\sqrt{4\pi f_{\rm m}(r,\theta)/v_{\rm r}}, \tag{20}$$

where $v_{\rm r} \simeq c$ is the radial wind velocity.

The Lorentz factor of the Crab's pulsar wind, as well as its angular dependence, is not known but is expected to be very high, in the range $\Gamma = 10^2$–10^6. Our 3D code simply cannot cope with such high values. For this reason, we adopt the much lower value $\Gamma = 10$ for all its streamlines, like in the previous axisymmetric studies (e.g. Komissarov & Lyubarsky 2004; Camus et al. 2009).

The wind rest mass density can be found via

$$\rho(r,\theta) = f_{\rm k}(r,\theta)/(\Gamma^2 c^2 v_{\rm r}). \tag{21}$$

In spite of the apparent dramatic mismatch between the real and simulated wind Lorentz factors, we do not expect this to make a significant impact on the PWN dynamics. Indeed, according to equation (21), the kinetic energy flux depends only on the product $\Gamma^2\rho$. Moreover, the magnetization $\sigma = B^2/(4\pi\Gamma^2\rho c^2)$ depends only on the term $\Gamma^2\rho$ too. Hence, our models can be scaled to more realistic values of the wind Lorentz factor without changing the dynamical properties of the wind (ram pressure and magnetization) when the wind density is scaled according to $\rho \propto \Gamma^{-2}$. At the same time, the position of the termination shock (TS) is determined by the ram pressure balance and will be the same as in our simulations. In order to verify this conclusion, we have performed low-resolution

Downloaded from http://mnras.oxfordjournals.org/ at University of Leeds on April 1, 2016

2D test simulations with the wind Lorentz factor as high as $\Gamma = 80$ and observed no significant change in the termination shock size.

2.3 Modelling of synchrotron emission

For the production of synthetic synchrotron maps (see Section 4), additional scalars are advanced with the flow. Following Camus et al. (2009), we assume the power-law distribution of leptons injected at the termination shock

$$f(\epsilon) = A\, n_0 \epsilon^{-p} \qquad \text{for} \qquad \epsilon < \epsilon_{\infty,0}, \tag{22}$$

where $\epsilon_{\infty,0}$ is the cutoff energy of the injected particles, chosen to be 1 PeV at every point of the shock, n_0 is their number density and A is the normalization constant. We set $p = 2.2$, as this value was found best suited to approximate the synchrotron spectrum of the Crab from the optical to X-ray frequencies in a number of previous studies (Kennel & Coroniti 1984b; Atoyan & Aharonian 1996; Volpi et al. 2008). Assuming that downstream of the termination shock these particles are subject to the synchrotron and adiabatic energy losses only, their local energy spectrum is given by

$$f(\epsilon) = A\, n_0 \left(\frac{n_0}{n}\right)^{-\frac{2+p}{3}} \left(1 - \frac{\epsilon}{\epsilon_\infty}\right)^{p-2} \epsilon^{-p}\,, \ \epsilon < \epsilon_\infty. \tag{23}$$

In this equation, ϵ_∞ is the local cutoff energy and n is the local number density of the particles. The evolution of these parameters is described by three additional conservation laws, which are integrated simultaneously with the main RMHD system.

The first two are the continuity equation for n

$$\frac{\partial}{\partial t}(n\Gamma) + \nabla_i(n\Gamma v^i) = 0, \tag{24}$$

and the advection equation for n_0

$$\frac{\partial}{\partial t}(n_0 n\Gamma) + \nabla_i(n_0 n\Gamma v^i) = 0. \tag{25}$$

In terms of the comoving total time derivative $\mathrm{d}/\mathrm{d}t' = \Gamma\,(\partial/\partial_t + \boldsymbol{v}\cdot\nabla)$, the evolution of ϵ_∞ is governed by

$$\frac{\mathrm{d}}{\mathrm{d}t'}\ln\epsilon_\infty = \frac{\mathrm{d}}{\mathrm{d}t'}\ln n^{1/3} + \frac{1}{\epsilon_\infty}\left(\frac{\mathrm{d}\epsilon_\infty}{\mathrm{d}t'}\right)_{\mathrm{S}}, \tag{26}$$

where the radiative loss term is given by

$$\left(\frac{\mathrm{d}\epsilon_\infty}{\mathrm{d}t'}\right)_{\mathrm{S}} = -\tilde{c}_2 B'^2 \epsilon_\infty^2 \tag{27}$$

(e.g. Del Zanna et al. 2006). Here, B' signifies the magnetic field as measured in the comoving frame and $\tilde{c}_2 = 4e^4/(9m_e^4c^7)$ denotes the second synchrotron constant for an assumed isotropic pitch angle distribution of particles (e.g. Pacholczyk 1970). As demonstrated by Camus et al. (2009), equation (26) can be cast in conservation form as

$$\frac{\partial}{\partial t}(\epsilon_\infty n^{2/3}\Gamma) + \nabla_i(\epsilon_\infty n^{2/3}\Gamma v^i) = -\tilde{c}_2 B'^2 \epsilon_\infty^2 n^{2/3}. \tag{28}$$

This is the third additional conservation law.

Since the termination shock is highly non-spherical and variable, the value of n_0 depends on the distance from the origin of the location where the fluid element crosses the shock. Since the pulsar wind is not spherically symmetric it should also depend on the polar angle of this location. The exact dependence is difficult to predict as it is influenced not only by the shock compression factor but also by the particle flux distribution in the pulsar wind and the efficiency of the particle acceleration at the termination shock, which are not well constrained at the moment. In the simulations, we introduce n_0 using the following prescription. In the pulsar wind zone, which is identified by its high Lorentz factor, we reset n_0 every time step to its prescribed value $n_{\mathrm{w}}(r, \theta)$. Everywhere else n_0 is computed according to the aforesaid evolution equations.

For n_{w} we investigate two recipes. In the recipe A

$$n_{\mathrm{w}} \propto r^{-2}. \tag{29}$$

Obviously, this recipe does not distinguish between the striped-wind zone and the polar zone, which is stripe free. In contrast, in the recipe B we assume that the synchrotron electrons (and positrons) are only accelerated at the termination shock of the striped wind:

$$n_{\mathrm{w}} \propto (1 - \chi_\alpha(\theta))\, r^{-2}. \tag{30}$$

This reflects the results of recent studies of collisionless relativistic shocks, which indicate very low efficiency of particle acceleration at such shocks when the angle between the shock normal and the magnetic field is sufficiently large, the so-called superluminal shocks (Sironi & Spitkovsky 2009). However, in the case of striped wind, the particle acceleration may still operate downstream of the MHD shock, in the region where the alternating magnetic field of the stripes is dissipated (Lyubarsky 2003; Sironi & Spitkovsky 2011b).

Note that this is a purely passive treatment in the sense that we neglect the influence of radiative cooling on the flow dynamics. Normally, this is justified by the fact that the Crab nebula total luminosity is only $\simeq$10 per cent of the spin-down luminosity of the Crab pulsar (e.g. Del Zanna et al. 2006). However, as discussed by Foy (2007), locally the impact of radiative losses can be quite high. For example, the Crab wisps may lose up to 30 per cent of their energy. We plan to explore this further in a subsequent paper. Another shortcoming of this approach is that it ignores the potentially important particle acceleration inside the nebula, which is related to its turbulence and magnetic reconnection.

Given the lepton spectrum (23), the synchrotron emissivity in the observer frame is

$$j_\nu \propto \mathcal{C} \begin{cases} \nu^{\frac{1-p}{2}} \left(1 - \sqrt{\frac{\nu}{\nu_\infty}}\right)^{p-2}; & \nu < \nu_\infty \\ 0; & \nu > \nu_\infty \end{cases} \tag{31}$$

where

$$\mathcal{C} = n_0 \mathcal{D}^{2+(p-1)/2} B_\perp'^{(p/2+1/2)} \left(\frac{n_0}{n}\right)^{-\frac{p+2}{3}}$$

and

$$\mathcal{D} = \frac{1}{\Gamma(1 - \boldsymbol{\beta}\cdot\boldsymbol{n})} \tag{32}$$

is the Doppler factor. The cutoff frequency is defined as $\nu_\infty \equiv c_1 B'_\perp \epsilon_\infty^2$ with the synchrotron constant $c_1 = 3e/(4\pi m_e^3 c^5)$. Note that the emissivity depends on the magnetic field component perpendicular to the line of sight vector $\boldsymbol{n}'$ in the comoving system (indicated by dashes): $B'_\perp \equiv |\boldsymbol{B}' \times \boldsymbol{n}'|$ which is obtained via the Lorentz transformation. Optically thin intensity maps are then obtained via the straight forward integration

$$I_\nu(x, y) = \int_{-\infty}^{\infty} \mathrm{d}z\; j_\nu(x, y, z) \tag{33}$$

in Cartesian coordinates where the z direction is aligned with the line of sight. To obtain the linear polarization degree and direction, we additionally solve the radiation transport equations for the Stokes

Downloaded from http://mnras.oxfordjournals.org/ at University of Leeds on April 1, 2016

parameters Q and U via

$$I_\nu^p(x,y) \equiv Q(x,y) + iU(x,y) \tag{34}$$

$$= \frac{p+1}{p+7/3}\int_{-\infty}^{\infty} \mathrm{d}z\, j_\nu(x,y,z) e^{2i\chi(x,y,z)}. \tag{35}$$

This is analogous to the method described by Del Zanna et al. (2006). In this equation, χ is the local angle of the newly emitted photons electric field $\boldsymbol{e}$, as measured in the observer frame with respect to the y-axis in the plane of the sky. Theory of relativity introduces a swing of the polarization angle, which is similar to the relativistic aberration effect (Blandford & Königl 1979; Porth et al. 2011). The radiation electric field in the observer frame is given by

$$\boldsymbol{e} \propto \boldsymbol{n} \times \boldsymbol{q}; \qquad \boldsymbol{q} = \boldsymbol{B} + \boldsymbol{n} \times (\boldsymbol{\beta} \times \boldsymbol{B}), \tag{36}$$

where all quantities are measured in the observer frame (Lyutikov, Pariev & Blandford 2003). Hence χ is determined from

$$\cos\chi = \hat{\boldsymbol{y}} \cdot \hat{\boldsymbol{e}}\,; \qquad \sin\chi = \boldsymbol{n} \cdot (\hat{\boldsymbol{y}} \times \hat{\boldsymbol{e}}), \tag{37}$$

where $\hat{\boldsymbol{v}}$ is the unit vector in direction of $\boldsymbol{v}$. Note that χ increases counter-clockwise. From the above Stokes parameters, the degree of linear polarization is

$$\Pi_\nu = \frac{\sqrt{Q_\nu^2 + U_\nu^2}}{I_\nu} = |I_\nu^p|/I_\nu, \tag{38}$$

which has a maximal value of $(p+1)/(p+7/3) \simeq 0.706\,(p=2.2)$. In this notation, the photon e-field direction is simply given by the real and imaginary part of $\sqrt{I_\nu^p}$,

$$e_x = -\Im\sqrt{I_\nu^p} \tag{39}$$

$$e_y = \Re\sqrt{I_\nu^p}. \tag{40}$$

2.4 Analytical reference model

In the classical paper on the Crab nebula by Kennel & Coroniti (1984b), one of the main observational constraints on the MHD model is the size of its termination shock. During the phase of self-similar expansion, which is appropriate given the current age of the nebula, it is a roughly constant fraction of the nebula size.

Given the initial setup, all our solutions exhibit two distinct phases. During the first phase, the initial discontinuity at r_i splits into three waves and the termination shock rapidly moves inwards, reflecting the build-up of the shocked PWN plasma. During the second phase, the shock re-bounces and begins to expand, at a much slower rate, towards its asymptotic self-similar position. Unfortunately, the computational cost of actually reaching the self-similar phase in 3D simulations is prohibitive and this complicates testing of our numerical models against both the observations and the above-mentioned analytical models. To overcome this problem, we decided to look for a simple 1D analytical solution describing the transition to the self-similar regime. To this end, we considered the adiabatic spherically symmetric expansion of PWN powered by an unmagnetized wind. Since the analytical models suggest very low wind magnetization (Rees & Gunn 1974; Kennel & Coroniti 1984a), the unmagnetized case turns out to be quite suitable here.

Assuming the polytropic equation of state with $\gamma = 4/3$ and a radial power law for the expanding nebula radius $r_\mathrm{n} = r_\mathrm{i}(t/t_0)^{\alpha_\mathrm{r}}$, we find that the evolution of the PWN energy E is governed by the equation

$$\dot{E} = L - \alpha\frac{E}{t}. \tag{41}$$

Given the initial condition $E(t_0) = 0$, the solution to this equation is

$$E = \frac{Lt}{1+\alpha}\left(1 - \left(\frac{t_0}{t}\right)^{\alpha_\mathrm{r}+1}\right). \tag{42}$$

The velocity of the accelerating nebula boundary is then $v_\mathrm{n} = \alpha_\mathrm{r} r_\mathrm{n}/t$ and when we set $t = 0$ as the time of the supernova, $t_0 = \alpha_\mathrm{r} r_\mathrm{i}/v_\mathrm{i}$ corresponds to the initial time of the simulations.

From the momentum conservation at the termination shock, one finds the characteristic shock size (see Appendix A)

$$r_0 = \left(\frac{L}{4\pi pc}\right)^{1/2} \tag{43}$$

and hence

$$r_0 = (1+\alpha_\mathrm{r})^{1/2}\alpha_\mathrm{r}^{-1} r_\mathrm{n}(v_\mathrm{n}/c)^{1/2}\left(1 - \left(\frac{t_0}{t}\right)^{\alpha_\mathrm{r}+1}\right)^{-1/2}. \tag{44}$$

This equation tells us that the time-scale of the transition to the self-similar expansion corresponds to a simulated time of t_0, which is $\simeq \alpha_\mathrm{r}\,210\,\mathrm{yr}$ for our parameters.

For the angular dependence of the wind energy flux utilized in our simulations, $f_\mathrm{tot}(\theta) \propto \sin^2\theta$, the maximal radial and vertical extents of the termination shock in this reference model are

$$r_\mathrm{max} \simeq 0.825\, r_0 \quad \text{and} \quad z_\mathrm{max} \simeq 0.232\, r_0 \tag{45}$$

(see Appendix A). As argued by Bucciantini et al. (2003, 2004), the equation of motion for the PWN radius in fact depends only on the total pressure at the nebula boundary, rendering the expansion law r_n independent of magnetization. We can hence utilize the hydrodynamic results obtained by means of the thin shell approximation for the forward PWN shock (e.g. van der Swaluw et al. 2001) and use the resulting index $\alpha_\mathrm{r} = 6/5$ as our reference value.

Kennel & Coroniti (1984b) used $v_\mathrm{n} = 2000\,\mathrm{km\,s^{-1}}$ and deduced the radius of Crab's termination shock to be $r_\mathrm{s} = 0.056\, r_\mathrm{n}$. Following the high-resolution *Chandra* observations reported by Weisskopf et al. (2000), it seems natural to identify the equatorial size of the termination shock with that of the Crab's X-ray inner ring, $r_\mathrm{ir} \sim 0.14\,\mathrm{pc}$. Adopting the volume averaged nebula radius of $r_\mathrm{n} = 1.65\,\mathrm{pc}$ (Hester 2008), we obtain $r_\mathrm{s} = 0.085\, r_\mathrm{n}$, slightly larger than the Kennel & Coroniti (1984b) value. If we plug the above value for v_n into equations (44) and (45) for $t \gg t_0$, we obtain $r_\mathrm{max}/r_n = 0.083$, which is actually in a very good agreement with the observed ratio! This suggests that we may consider our 3D numerical magnetic models of PWN as being in agreement with the observations if they do not differ much from our non-magnetic analytical model. According to equation (6), the initial expansion speed in our simulations is set to $v_\mathrm{i} \simeq 1500\,\mathrm{km\,s^{-1}}$, which lets room for a moderate acceleration over the nebula history.

3 RESULTS

3.1 Global energy balance

In our analysis of the energy balance of simulated PWN, we distinguish between the magnetic, kinetic and thermal energy densities which are defined as follows:

$$e_\mathrm{m} \equiv \frac{B^2 + E^2}{8\pi}, \tag{46}$$

Downloaded from http://mnras.oxfordjournals.org/ at University of Leeds on April 1, 2016

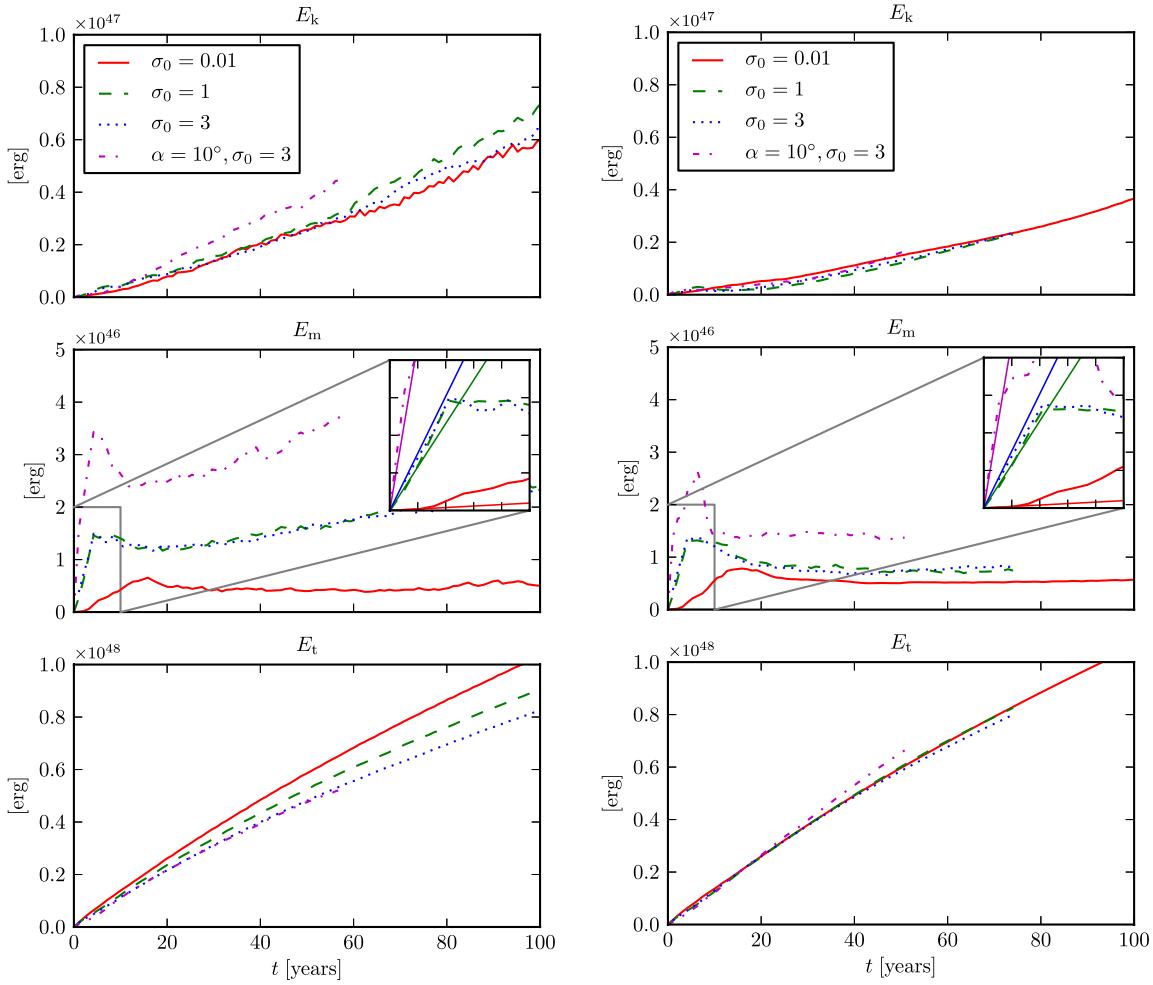

Figure 2. Evolution of the total kinetic, E_k, magnetic, E_m and thermal energy E_t of the nebula. The left-hand panels show the results of 2D runs {A2D, B2D, C2D, D2D}, whereas the right-hand panels show the 3D results for the models with equivalent setups {A3D, B3D, C3D, D3D}. The insets in the magnetic energy plots (second panel) compare the naive expectation $L_{m,s}t$ (straight lines) with the actual data.

$$e_k \equiv (\Gamma - 1)\,\Gamma \rho c^2, \tag{47}$$

$$e_t \equiv 4\Gamma^2 p - p. \tag{48}$$

The PWN volume is distinguished from that of the supernova shell by means of the passive scalar tracer $\tau \in [0, 1]$, which is advected along with the flow. In the pulsar wind, we set $\tau = 1$, and in the initial solution, $\tau = 0$ for $r > r_i$. Using this tracer, the PWN volume is determined by the integral

$$V_{PWN} = \int \Theta(\tau - 10^{-3})\,\Theta(9 - \Gamma)\,dV\,, \tag{49}$$

where $\Theta(\,\cdot\,)$ is the Heaviside step function. The second step function in this equation is introduced in order to exclude the unshocked wind zone from the nebula test volume.

The evolution of the energies in our simulations is shown in Fig. 2. It is interesting to view the nebula magnetic energy content in relation to the injected power $L_{m,s}$. Its initial evolution depends mainly on the wind magnetization. In the cases with high magnetization, $\sigma_0 \geq 1$, we simply have $E_m \simeq L_{m,s}t$, whereas in the low-σ case E_m grows faster (see the inserts in Fig. 2). The possibility of such odd evolution for low-σ models has been discussed in Rees & Gunn (1974) – the magnetic energy grows at the expense of the thermal energy as work is carried out against the magnetic hoop stress.

During this initial period the magnetic flux is conserved. 5 to 10 yr after the start of the simulations, the turbulence in the PWN is sufficiently developed and the magnetic dissipation begins to influence the evolution of E_m. At this stage, the magnetic energy in the 2D cases continues to rise slowly, whereas it levels off in the 3D realizations.[1] Extrapolating from the simulations, we expect today's Crab nebula to contain a total energy of $\simeq 10^{49}$erg in good agreement with the previous estimates (e.g. Hester 2008).

3.2 Global structure

One of the most striking features of the previous 2D axisymmetric simulations of PWN is their strong axial compression due to the hoop stress of their purely azimuthal magnetic field. These results agree very well with the theoretical models of the z-pinch configurations of PWN by Begelman & Li (1992). With the increased

[1] Since our 3D runs have not reached the phase of self-similar expansion, they cannot be used to deduce the long-term evolution on the scale of the Crab nebula lifetime.

Downloaded from http://mnras.oxfordjournals.org/ at University of Leeds on April 1, 2016

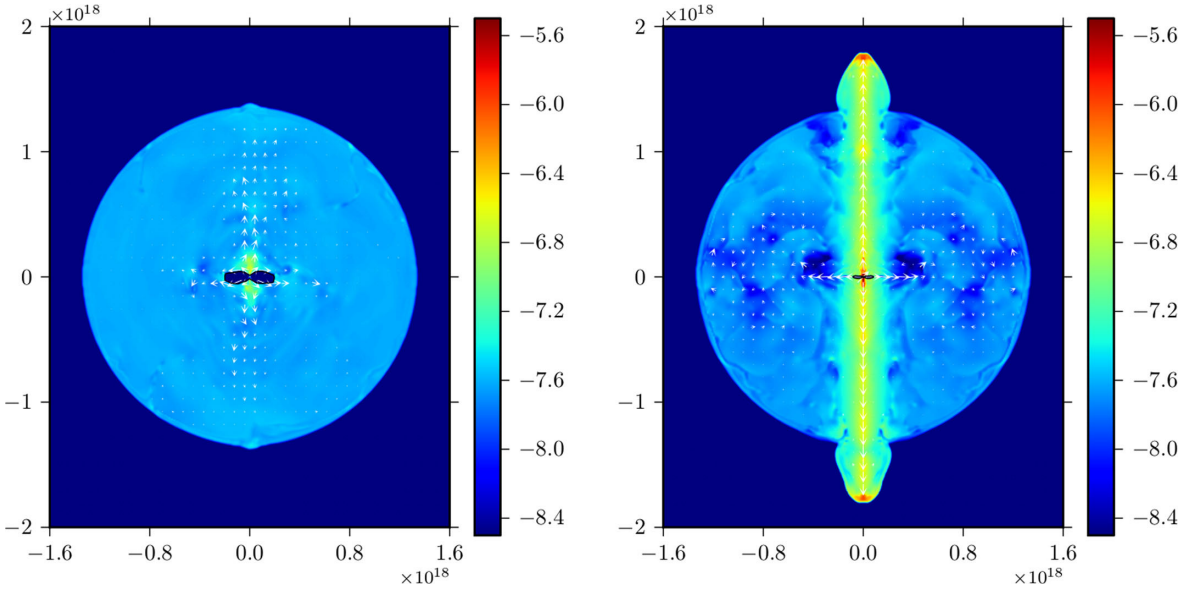

Figure 3. Dependence of the total pressure distribution, $\log_{10} p_{\rm tot}$, on the imposed symmetry. The left-hand panel shows the pressure distribution in the *xz* plane of the 3D simulation run B3Dhr and the right-hand panel in the corresponding 2D run B2Dhr, both at the time of 51 yr from the start of the simulations. The white arrows show the in-plane velocity vectors. The strong axial compression observed in this and previous 2D simulations is an artefact of the imposed symmetry.

magnetization of the pulsar wind, the pressure distribution over the interface with the supernova shell becomes so much enhanced near the polar region that the nebula expansion in the polar direction becomes significantly faster compared to the one in the equatorial direction. The polar jets begin to drill holes through the supernova shell and produce escape routes for the PWN plasma (see the right-hand panel of Fig. 3). Such breakouts have been observed in similar earlier simulations, aimed to explain the origin of GRB jets in the magnetar model (Bucciantini et al. 2007, 2008).

In contrast, the additional degree of freedom in our 3D simulations allows a fairly uniform distribution of the total pressure in the nebula (see the left-hand panel of Fig. 3). Thus, the assumption that the PWN plasma adopts a magnetohydrostatic z-pinch configuration as proposed in Begelman & Li (1992) is an oversimplification. The symmetry of the pulsar wind is not preserved inside the nebula due to kink instability of this configuration (see Section 3.7). Only in the very vicinity of the termination shock, which is dominated by the plasma injected into the nebula recently, we still observe a noticeable axial compression. This is the formation region of the polar jets (plumes).

3.3 Evolution of the termination shock

To investigate whether the observational constraint on the termination shock size can be satisfied, we now focus on the temporal evolution of the shock. Given the fact that in the simulations the shock shape can be quite complex compared to that of our simple analytical model, we need to come up with a robust procedure for measuring its sizes. The sizes given below are measured as follows. First, a rectangle is fitted around the unshocked wind region as shown in Fig. 4. Then the horizontal and vertical lengths of this rectangle are identified with doubled $r_{\rm max}$ and $z_{\rm max}$, respectively.

The results are shown in Fig. 5, together with the prediction of our reference analytic model (44). The most striking and important result is that the shock sizes in 3D runs with high wind magnetization and $\alpha = 45^\circ$ follow very closely the analytical curves, even better than the model with $\sigma_0 = 0.01$. This is in great contrast with

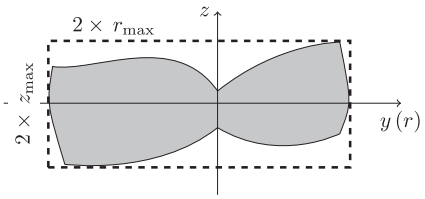

Figure 4. Sketch of the termination shock. The shock size is measured in the *yz* plane by fitting the wind region into a rectangle with base lines $2r_{\rm max}$ and $2z_{\rm max}$.

the Kennel & Coroniti (1984a) model, where for such high magnetizations the shock size collapses to zero. Moreover, as the initial magnetization σ_0 increases from 1 to 3, the shock size remains virtually unchanged. This is not overly surprising, given that the energetically most important parameter $\bar{\sigma}_{\rm s}$ (see Table 1) changes only by ∼40 per cent. In our 2D simulations, the agreement with the reference model is not as good but can still be considered as satisfactory, with deviations within a factor of less than 2.

As expected, the difference between the mean shock sizes in 2D and 3D simulations is particularly minor in the models with $\sigma_0 = 0.01$. However, the short-term variability of the shock is much more pronounced in the 2D case, indicating that the symmetry condition promotes this variability. On the other hand, the fact that in 3D simulations the shock variability is strong for models with high σ_0 and almost absent in the model with $\sigma_0 = 0.01$ shows that the magnetic field plays a key role in exciting and sustaining this variability.

For magnetizations $\sigma_0 \geq 1$, the difference between 2D and 3D results becomes stronger, resulting in shock sizes which are ∼1.5 times larger in radial direction and ∼2 times larger in vertical direction in the 3D models compared to the corresponding 2D models. This is consistent with the lower axial compression of the nebula in the 3D solutions as described in Section 3.2. As a further consistency check, we run simulations with the obliqueness $\alpha = 10^\circ$, which gives higher magnetization of the plasma supplied

Downloaded from http://mnras.oxfordjournals.org/ at University of Leeds on April 1, 2016

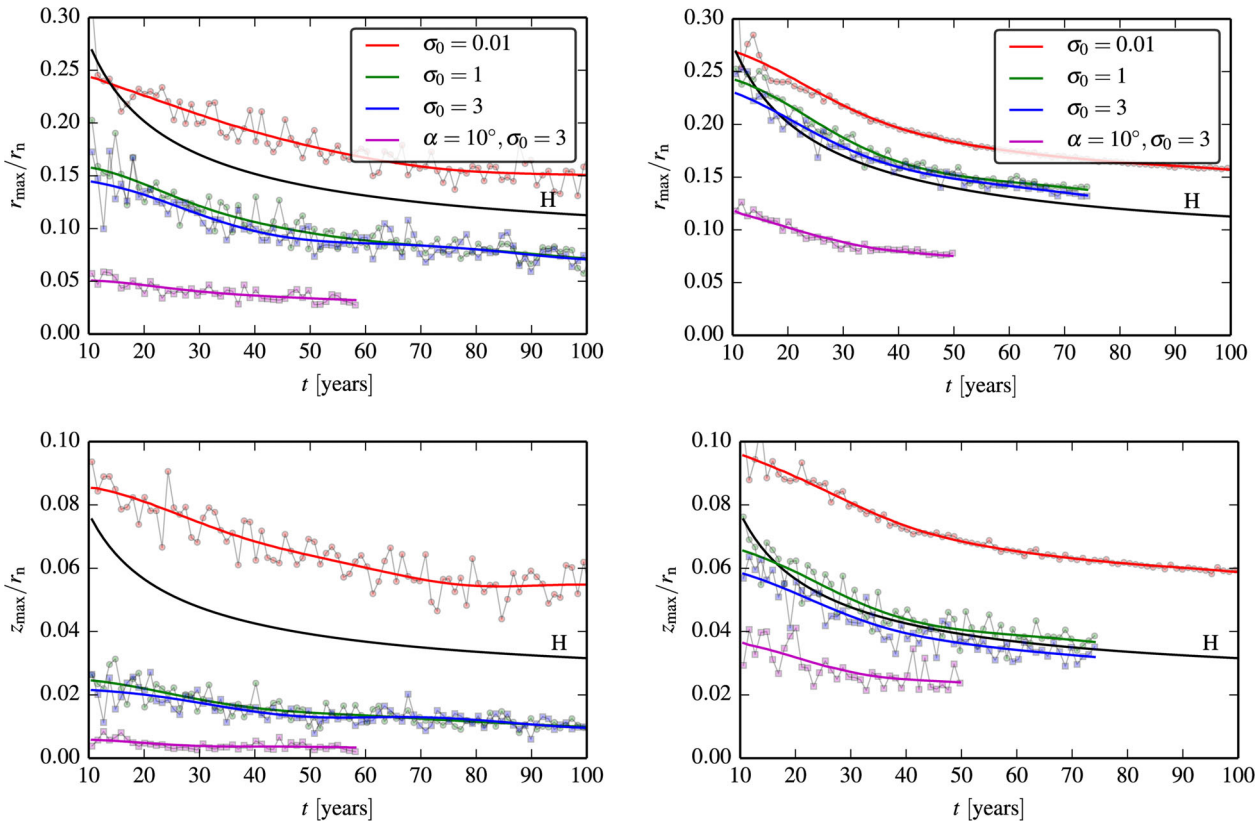

Figure 5. Maximum horizontal and vertical extent of the TS in units of the volume averaged nebula radius. The left-hand panels show the 2D runs for models {A2D, B2D, C2D, D2D} while the 3D results with the equivalent setups {A3D, B3D, C3D, D3D} are shown in the right-hand panels. The smooth lines show the low-pass filtered data and hence illustrate the overall long-term trend. The markers show the actual shock size and hence illustrate the short-term shock variability. The hydrodynamic expectation based on equation (44) is given by the black solid line labelled with letter 'H'.

into the nebula and hence promotes stronger axial compression. As expected, in these runs we obtained smaller termination shocks.

Fig. 6 illustrates the typical flow behaviour in the vicinity of the termination shock in the 3D simulation B3Dhr. One can see that this 3D solution reproduces the typical morphology seen in the earlier 2D simulations (Komissarov & Lyubarsky 2004), with its Mach belt, polar compression region, rim shock and the fast 'ϒ-flow' just outside of the oblique section of the termination shock. This figure also shows the vortex shedding by the termination shock. The vortices are formed near the Mach belt and then move outwards. The newly formed vortices seem to interact with the termination shock, modulating the width of its Mach belt. For example, in the first panel, which features strong vortices near the Mach belt, its width is much smaller than in the fourth panel, which shows no strong vortices close to the termination shock. The figure also shows very irregular and highly variable total pressure and velocity fields in the immediate surrounding of the shock, thus exposing the highly dynamic nature of the PWN flow in this region. It is not surprising that the termination shock responds to this flow by changing its shape.

On the other hand, the unsteady termination shock itself is a source of variable downstream outflow, seeding waves, shocks and vortices into the nebula. For example, as the shock obliqueness increases due to its vertical compression, the downstream flow velocity also increases (obeying the jump conditions) and a feedback cycle is established. This quasi-periodic nature of the TS was discussed by Camus et al. (2009), who commented on the difficulty in distinguishing the cause and effect of the shock perturbations.

The most significant difference between the 2D and 3D simulations is in the nature of the axial compression and its impact on the termination shock. In the 2D simulations, waves converge on the symmetry axis in a highly coordinated way, creating very strong variability of the total pressure right at the funnel of the termination shock and having very strong impact on the shock size along the axis. In the 3D simulations, the non-axisymmetric instabilities disrupt the highly coordinated structure of the 2D flow near the polar axis. The total pressure does not display such a strong maximum at the axis and the amplitude of its variability is reduced. A much more extended region of enhanced pressure around the axis is created instead. This explains the somewhat lower amplitude of the shock radius variations in the 3D simulations (cf. Fig. 5). With these differences in mind, we find that the mechanism of coupling the shock perturbations to the variations in the nebula flow still operates in the full 3D case and results in substantial variations on less than one year time-scale.

3.4 Magnetic dissipation in the nebula

Surprisingly, even the 2D cases show an acceptable shock size when compared to the Crab nebula observations via our analytic reference model. This is due to the dissipation of the nebula magnetic field, which occurs when loops of opposite polarity come together in the turbulent nebula flow. Its overall effect on the nebula energetics is demonstrated by Fig. 7 which shows the ratios of the magnetic to the kinetic and thermal energies in the nebula.

Downloaded from http://mnras.oxfordjournals.org/ at University of Leeds on April 1, 2016

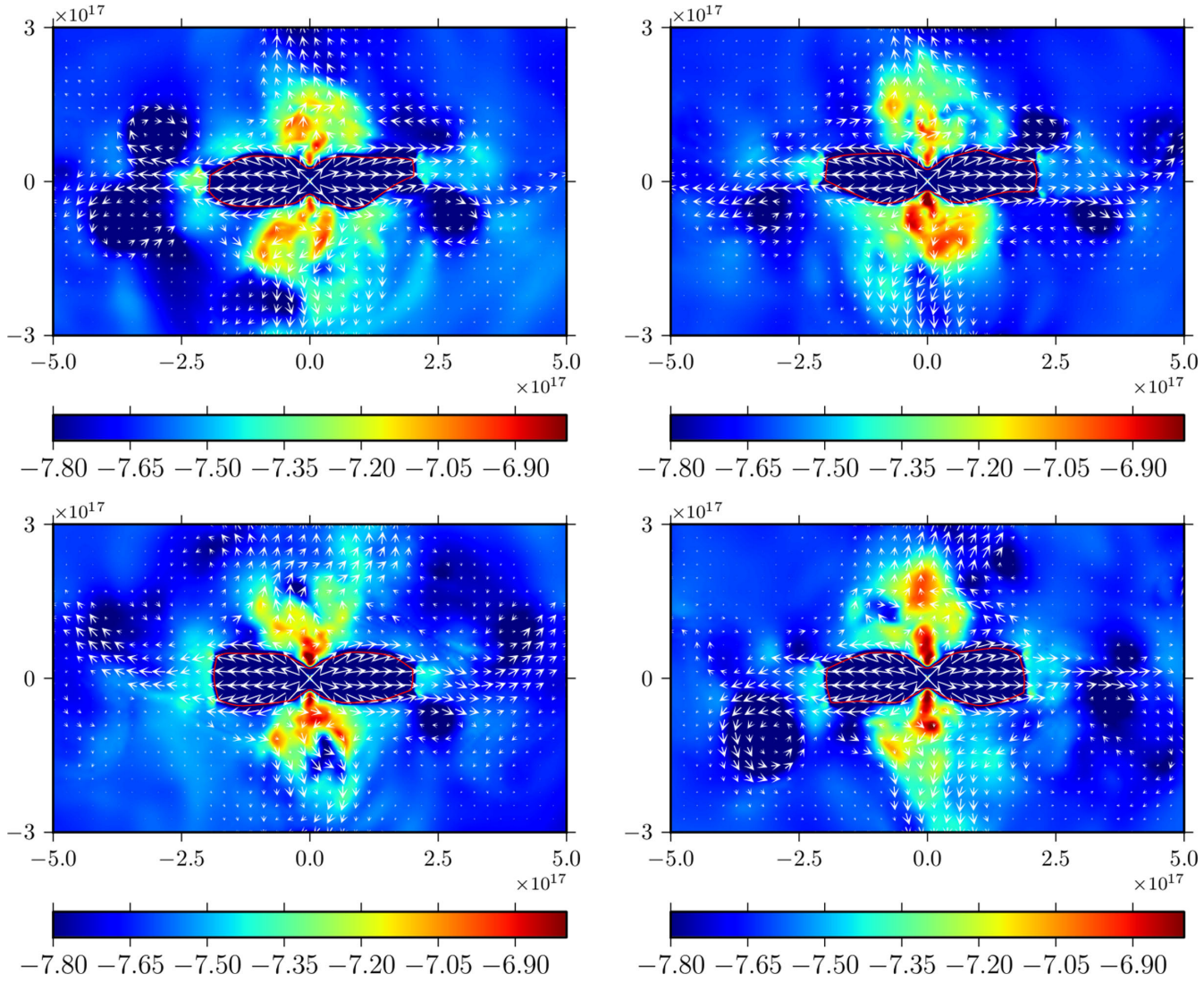

Figure 6. Variability of the termination shock in the 3D simulation B3Dhr. The colour images show the logarithm of total pressure $\log_{10} p_{\rm tot}$ in the xz plane and the in-plane velocity vectors are shown as white arrows. The red line shows the location of the termination shock. The snapshots are taken at $t = 44$, 45, 46, 47 yr (left to right, top to bottom). One can take the quasi-periodic vortex shedding from the termination shock and its distortion by the highly variable PWN flow.

One can see that all simulations follow rather similar evolution of $E_{\rm m}/E_{\rm k}$, the ratio of magnetic and kinetic energies. At the start of the simulations, $E_{\rm m} \simeq 10\,E_{\rm k}$ and after 100 yr, $E_{\rm m} \lesssim E_{\rm k}$.

The results for $E_{\rm m}/E_{\rm t}$ are even more conclusive. If the magnetic field was only randomized, as suggested by Begelman (1998), but not subject to significant dissipation then one would expect this ratio to remain unchanged during the nebula lifetime. Because the magnetic hoop stress is no longer significant, the randomized magnetic field behaves like an ultrarelativistic ideal gas (Heinz & Begelman 2000) and hence evolves in the same way as the real gas of particles. Hence, $E_{\rm m}/E_{\rm t}$ stays the same. From Fig. 7 it is evident that our numerical solutions do not fully support the Begelman's hypothesis as in addition to the randomization a significant amount of magnetic energy is converted into the thermal energy of plasma. Obviously, this energy exchange between the two 'gases' does not have a direct impact on the global flow dynamics – it remains governed by the equations of relativistic hydrodynamics. Importantly, the magnetic dissipation does not require complete randomization of the field which would be difficult to reconcile with the observations. At least in the central parts, the optical polarization measurements (Schmidt, Angel & Beaver 1979; Hickson & van den Bergh 1990) clearly indicate dominance of the azimuthal component.

Lyutikov (2010) argued that the Crab nebula flow remains largely axisymmetric and the opposing magnetic loops meet at the equator and the polar axis, which become places of strong magnetic dissipation. However, even in our 2D simulations the situation is rather different as the so-called equatorial current sheet quickly leaves the equator and densely fills most of the nebula volume, being tangled by its turbulent eddies (see Fig. 8). Thus, the magnetic dissipation occurs over most of the nebula volume.

As to the polar region, in the 2D simulations it is occupied by the polar jet which is shielded from the rest of the nebula by its backflow and is almost free from the magnetic dissipation (see Fig. 8). In the 3D simulations, the situation is qualitatively different as no strong jet and backflow develop (we discuss the 'plume' further in Section 3.7). The non-axisymmetric motions of the plasma in the polar region promote displacement of magnetic loops and create additional sites of magnetic dissipations there. This is why the

Downloaded from http://mnras.oxfordjournals.org/ at University of Leeds on April 1, 2016

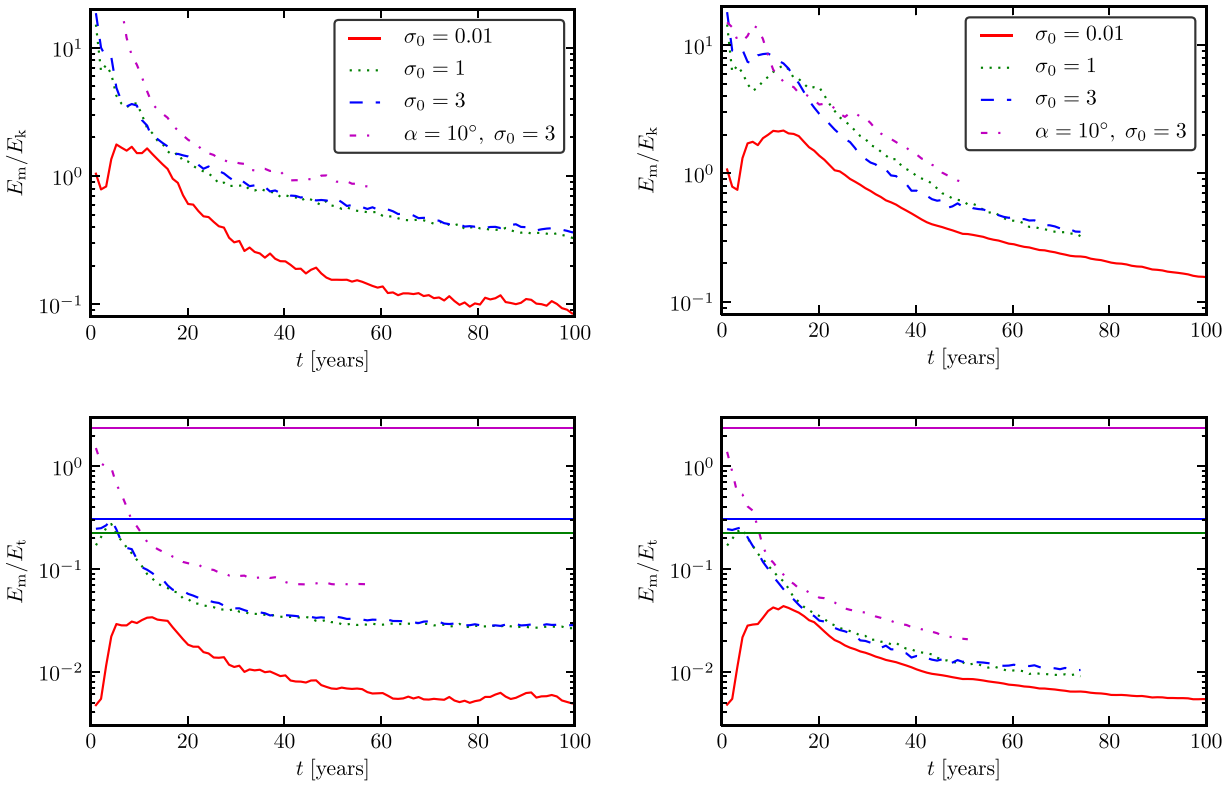

Figure 7. Magnetic dissipation in 2D and 3D simulations. The top panels show the ratio of the total magnetic and kinetic energies, whereas the bottom ones the ratio of total magnetic and thermal energies. The data from the 2D runs {A2D, B2D, C2D, D2D} are shown in the left-hand panels while the 3D results for the runs with the equivalent setups {A3D, B3D, C3D, D3D} are in the right-hand panels. The solid horizontal lines of the lower panels show the values expected in the case when the randomization of magnetic field is not accompanied by its dissipation.

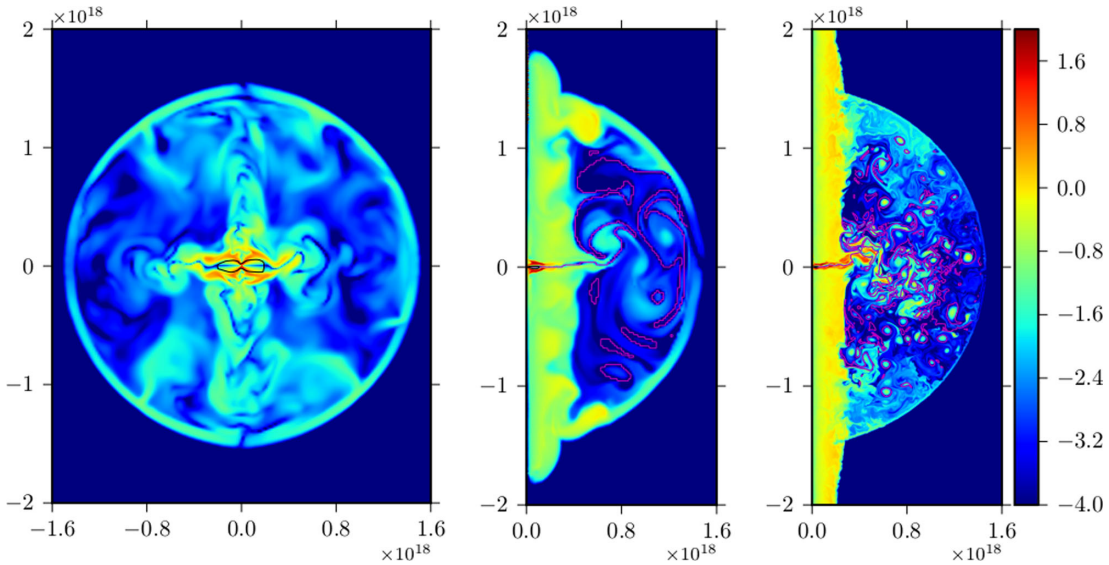

Figure 8. Magnetic dissipation regions in 3D and 2D simulations. The images show the distribution of $\log_{10} e_\mathrm{m}/e_\mathrm{t}$ for the models with $\alpha = 45^\circ$ and $\sigma_0 = 1$ at $t = 70$ yr. From left to right: the yz slice for the run B3D, the data for B2D and B2Duhr (the B2Duhr run has eight times higher resolution inside the nebula compared to B2D). The magenta line in plots for the 2D runs shows the locus of points where the magnetic flux changes its sign and the black contour shows the termination shock. In the 2D cases, a strong polar jet develops, which is shielded from the rest of nebula by its backflow.

magnetic dissipation is stronger in 3D. For example, the 3D models with $\alpha = 45^\circ$ and $\sigma_0 \geq 1$ reach $E_\mathrm{m}/E_\mathrm{t} \simeq 0.01$ by the time of $\sim$80 yr, whereas the corresponding 2D models seem to saturate at $E_\mathrm{m}/E_\mathrm{t} \simeq 0.03$ (see Fig. 7). Incidentally, the combined data on the synchrotron and inverse-Compton emission of the Crab nebula also lead to $E_\mathrm{m}/E_\mathrm{t} \simeq 0.03$ within its 'one-zone model'. This is in conflict with the much higher mean value expected on theoretical grounds for the plasma injected into the nebula by the pulsar wind

Downloaded from http://mnras.oxfordjournals.org/ at University of Leeds on April 1, 2016

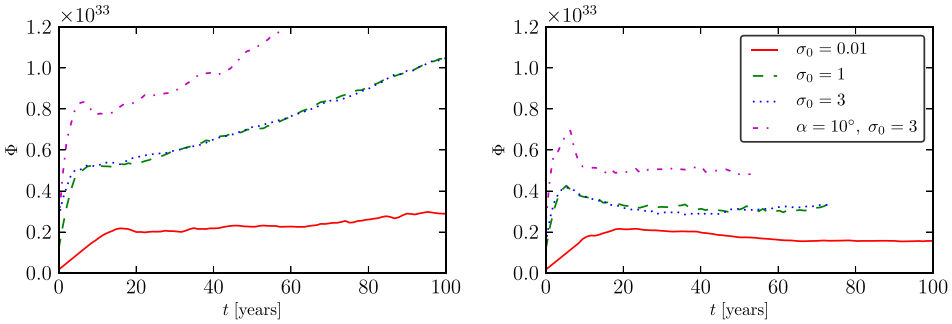

Figure 9. Evolution of the total azimuthal magnetic flux Φ as defined by equation (50). The left-hand panel shows the results for the 2D runs {A2D, B2D, C2D, D2D} while the results for the 3D runs with equivalent setups {A3D, B3D, C3D, D3D} are shown in the right-hand panel. The evolution departs from the flux conservation law after few light crossing times. In the 3D runs the flux saturates, whereas in the 2D runs it keeps increasing at approximately linear rate.

and hence suggestive of efficient magnetic dissipation inside the nebula (Komissarov 2013).

Since we integrate equations of ideal RMHD, the magnetic dissipation occurs at the grid scale via numerical resistivity. However, to become efficient it requires creation of ever smaller scale structures in the magnetic field distribution. The processes which drive the development of such structures, and occur on scales above the grid scale, must ultimately determine the dissipation rate and it is important that their dynamics is captured sufficiently accurately. The most stringent test we can perform to this end is to check the resolution dependence of the observables inferred from the simulations. This is described in detail in Appendix B and for the 3D simulations the results are encouraging: Upon doubling the resolution for the run B3D, we obtain very close results both for the termination shock size and the magnetic dissipation rate inferred from the nebula energetics. While the influence of the numerics cannot be ruled out completely yet (one has to wait until even higher resolution simulations become available and other numerical schemes tried) this lets us to believe that the high degree of dissipation observed in our simulations is not far from being realistic.

The combined observational data on the synchrotron and inverse-Compton emission of the Crab nebula lead to $E_m/E_t \simeq 0.03$, within its simplified 'one-zone model' (Meyer et al. 2010; Komissarov 2013). Our 3D data show saturation of this parameter around $E_m/E_t \simeq 0.01$ by the time of ∼80 yr, (see Fig. 7). This suggests that the magnetic dissipation in our simulations may be a bit excessive but not off the scale. On the other hand, the strength of magnetic field in our simulations is far from being uniform. In fact, in contrast to the 1D model of Kennel–Coroniti, it is significantly lower in the outskirts of the nebula compared to the vicinity of the termination shock. This raises questions about the reliability of estimates based on the one-zone model.

3.5 Azimuthal magnetic flux

The energy content of PWN is not solely determined by the magnetic dissipation and other dynamical factors may become important too. One may argue that a complimentary, and perhaps more direct, approach to quantification of the magnetic reconnection-driven dissipation should involve nebula's azimuthal magnetic flux.

In axisymmetry, the total azimuthal flux Φ contained within PWN can be defined via the integral

$$\Phi \equiv \int_S |B_\phi(r,\theta)| \mathrm{d}S \tag{50}$$

over any cross-section of the nebula containing the symmetry axis. In the absence of magnetic reconnection, this flux increases at the rate given by the flux injection rate of the pulsar wind. For a stationary wind this rate is constant. However, in the absence of axisymmetry, one has to specify a particular cross-section or to average over the azimuthal angle. Here, we simply measure the toroidal flux of the 3D runs in the yz plane. In any case, the resultant quantity is no longer conserved even in the absence of magnetic reconnection, which reduces the usefulness of this parameter.

The left-hand panel of Fig. 9 shows the temporal evolution of Φ in our 2D simulations. One can see that the flux does not increase at a constant rate but evolves through at least two phases. During the first phase the growth of Φ is linear and at the rate determined by pulsar wind. In the models with $\sigma_0 \geq 1$, this phase lasts for only few years, whereas in the low-σ model it continues for ∼15 yr. At the end of this phase, the nebula flow becomes fully turbulent, speeding up dramatically the annihilation rate of the magnetic flux. As the result, $\dot{\Phi}$ is significantly reduced. These two phases can also be seen in the plots of the magnetic energy evolution (see Fig. 2). In the 3D models, Φ remains approximately constant during the second phase (see the right-hand panel of Fig. 9). However, because the nebula expansion has not reached the self-similar phase, we cannot say that this is a characteristic of the long-term nebula evolution.

As we have commented above, the azimuthal flux is a less meaningful measure of magnetic reconnection in 3D models. Further progress in this direction could be made via procedures locating individual current sheets in the 3D data and measuring local energy conversion rate, for example by using an algorithm as proposed by Uritsky et al. (2010) and Zhdankin et al. (2013). We leave such an effort to future work employing higher spatial resolution as needed for the detection of the current sheets.

3.6 Magnetic field structure

Observations of optical polarized light from the Crab nebula indicate a rather complex magnetic structure. The early images of polarized intensity due to Michel et al. (1991) and Fesen, Martin & Shull (1992) revealed an 'hourglass' structure aligned in the north–south direction, which was interpreted as synchrotron emission originating in a predominantly azimuthal magnetic field. Near the nebula boundary the morphology is complex and indicative of a 'layered' configuration with the magnetic field wrapping around individual filaments (see the detailed account of Hester 2008). Thus, the observations suggest that the inner Crab nebula is dominated by the azimuthal component freshly supplied by the pulsar wind. In a 3D

Downloaded from http://mnras.oxfordjournals.org/ at University of Leeds on April 1, 2016

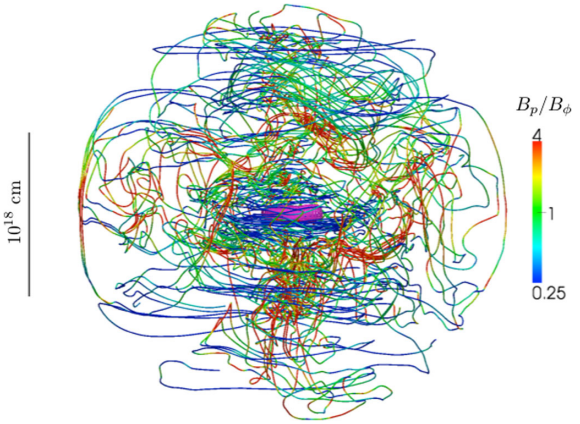

Figure 10. Field lines in the high-resolution run B3Dhr at $t = 50$ yr. The lines are coloured according to their orientation, sections with dominating azimuthal component being blue and those with dominating poloidal component red. In order to trace both the inner and the outer structure, the seed points of the field line integration are randomly placed on two spheres with radii of 4×10^{17} cm and 1.2×10^{18} cm. The surface of the termination shock is also shown, using the magenta contour.

flow, the non-axisymmetric effects such as the kink instability and 3D turbulence tend to randomize the magnetic field. Thus, the question is how quickly these processes destroy the ordered field in our simulations and whether their results agree with the observations in this respect.

Fig. 10 illustrates the typical complex magnetic field structure in the 3D simulated PWN. It is evident that with the loss of axisymmetry, the highly ordered structure of the magnetic field in the pulsar wind does not survive in the nebula where the field becomes fairly random. However, we can still identify regions of predominant field direction. For this purpose, we introduce the anisotropy parameter

$$\bar{\alpha} = \langle B_p^2/B^2 \rangle_\phi, \tag{51}$$

where the average is taken over the azimuthal direction. This quantity for the simulation run B3D shown in Fig. 11. One can see that the azimuthal component still dominates near the termination shock and that regions of predominantly *poloidal* field arise close to the jet and in the equatorial region next to the nebula boundary, where its magnitude is rather weak (see the right-hand panel of Fig. 11).

The magnetic field magnitude varies substantially throughout the simulated nebulae. The strongest field is found just outside of the termination shock, where it is roughly 10 times stronger compared to the mean field in the rest of the nebula volume (see the right-hand panel of Fig. 11). Comparing the left- and right-hand panels of Fig. 11, we find that regions of strong field are dominated by the azimuthal component (with a Pearson correlation coefficient between the anisotropy α and $|\boldsymbol{B}|$ of -0.17). This explains why the observed degree of polarization of the Crab nebula is so high near its centre and why the polarization vectors suggest azimuthal field.

3.7 Jet morphology

Perhaps the most interesting region in our simulations is the polar flow that is produced due to the hoop stress of the azimuthal field via the so-called toothpaste effect. This polar flow is strikingly different in 2D and 3D models.

The formation region of the polar flow in the 2D simulation run B2Dvhr is illustrated in Fig. 12. To better identify flow structure we show a close-up image of the size of the termination shock and

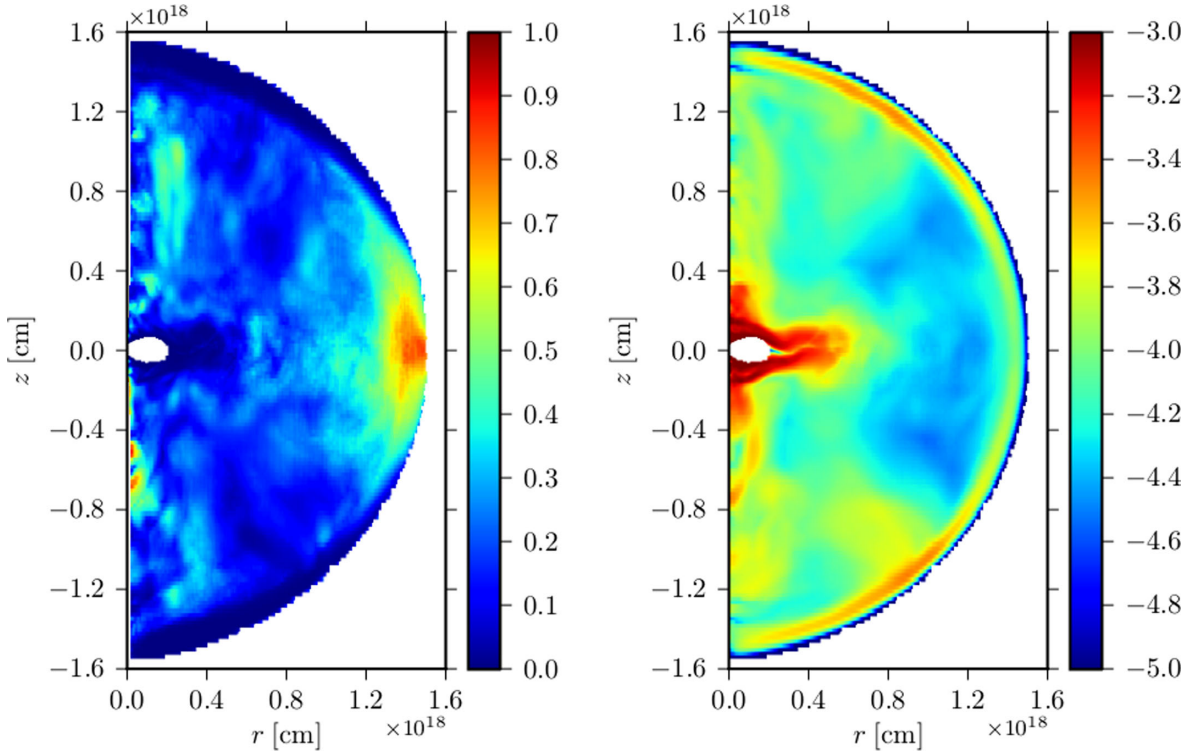

Figure 11. Anisotropy of the magnetic field and its strength in the simulation run B3D. The left-hand panel shows the parameter $\bar{\alpha} = \langle B_p^2/B^2 \rangle_\phi$ at the time $t \simeq 70$ yr. The right-hand panel shows the angular averaged field strength, $\log\langle |\boldsymbol{B}/1\,\mathrm{Gauss}| \rangle_\phi$, at the same time. The supernova shell and pulsar wind regions are not represented in the plots. The increase of the magnetic field strength near the outer radius of the PWN is probably an artefact.

Downloaded from http://mnras.oxfordjournals.org/ at University of Leeds on April 1, 2016

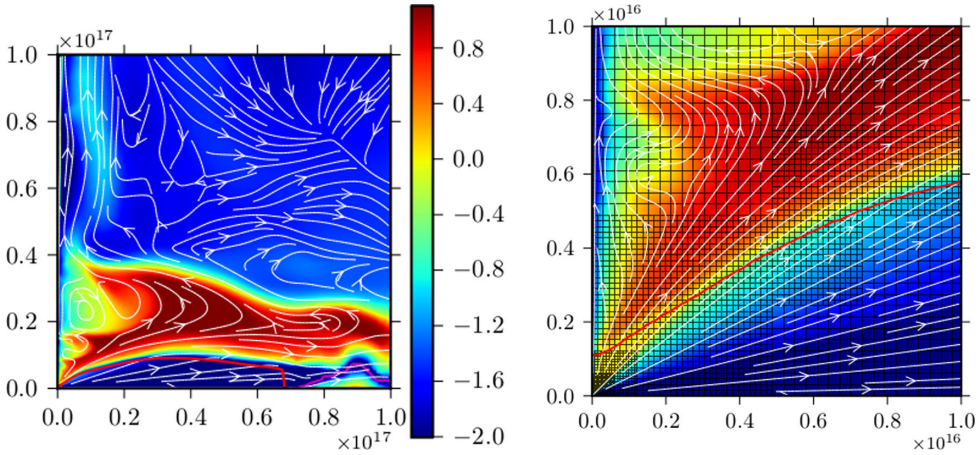

Figure 12. The flow structure near the termination shock in the axisymmetric model B2Dvhr at the time $t = 100$ yr from the start of the simulations. Left-hand panel: the colour image shows the generalized magnetization, $\log_{10}\sigma_s$. The 'momentary' stream lines show how the flow originating in the magnetized polar region becomes focused back towards the axis to form the jet. One can also see the jet backflow which provides additional compression of the termination shock. The red line shows the position of the termination shock whereas the magenta line shows the equatorial current sheet. Right-hand panel: as in the left-hand panel but for the very inner region. This plot also shows the computational grid. This illustrates the grid refinement at the termination shock and towards the origin. Note that the scale of this image is 100 times smaller than the radius of the initial nebula bubble.

also zoom on the flow near the very origin.[2] We find it helpful to distinguish two jet-like features: the 'polar beam' and the 'plume'. By the polar beam we understand the post-termination shock flow that is fed by the highly magnetized unstriped polar section of the pulsar wind. By the 'plume' we understand the polar outflow which formed by the axial collimation of the flow originating from the striped section of the pulsar wind. Surely, there is no discontinuity separating these wind sections, and hence the division between the beam and the plume is not sharp. This is only a matter of scales. Hence, the right-hand panel of Fig. 12 shows the dynamics of the polar beam, whereas the left-hand panel illustrates the formation of the plume. In particular, one can see the increase of the magnetization in the flow away from the symmetry axis until the magnetic hoop stress becomes strong enough to stop the expansion.

The linear stability analysis of axisymmetric z-pinch configurations of relativistic plasma, first performed by Begelman (1998), gives the time-scale for the fastest growing mode relevant to our application

$$t_g \sim \sqrt{\frac{4\pi\rho c^2}{B^2} + \frac{16\pi p}{B^2}}\,\frac{r}{c}, \tag{52}$$

where all quantities are measured in the comoving frame and r denotes the cylindrical radius. For a strong shock, the shocked flow is relativistically hot with $p \gg \rho c^2$ and the adiabatic index $\gamma = 4/3$. Hence,

$$t_g \sim (2\beta)^{1/2}\frac{r}{c}. \tag{53}$$

Since, t_g cannot be shorter than the light crossing time, this result only applies to plasma with $\beta > 1/2$. With the low-σ model of Rees & Gunn (1974) in mind, Begelman (1998) thus predicted that the azimuthal magnetic field will be disrupted at the distance $\sim 3r_s$ from the termination shock.

Lyubarsky (2012) argued that the stability of *collimating* flows is not adequately described by the Begelman (1998) model. Instead, he suggested that the polar beam becomes unstable at the re-collimation point

$$z_c = \frac{\pi}{\sqrt{6}}\theta_0^2 r_{\max}. \tag{54}$$

In the derivation, it was assumed that the initial opening angle of the beam is $\theta_0 \ll 1$.

The morphology of the polar beam in our 3D simulations is shown in Fig. 13 for the high-resolution run B3Dhr. Applying equation (53) to this case, we obtain the linear growth time-scale of $\sim 10^{-2}$ yr, much shorter than the light crossing time of the nebula. Given the grid resolution of 2.4×10^{15} cm at the termination shock, the flow is thus expected to become kink unstable after traversing only few grid cells. Indeed, the pressure isocontours of Fig. 13 appear heavily perturbed already on the scale of $\sim 10^{16}$ cm. The 'ridge' of the beam resembles a corkscrew, typical for the kink instability (e.g. Mizuno et al. 2009). The polar beam is thus highly variable and shifts orientation on less than monthly time-scales. This may be relevant to the rapid variability of the 'sprite' feature, which is located at the base of the Crab's X-ray jet (Hester et al. 2002).

If indeed the disruption of the beam follows its re-collimation then its maximal propagation length should be influenced by the opening angle of the unstriped region of the pulsar wind (see equation 54). We investigate this by comparing the simulation C3D featuring $\alpha = 45^\circ$ with the simulation D3D which has $\alpha = 10^\circ$. Both these runs are highly magnetized in the polar region ($\sigma_0 = 3$). Fig. 14 shows $\log_{10}\beta$ for these two cases, in the $x = 0$ plane, as well as the momentary stream lines of the velocity vector field (black lines) and the termination shock (red contour). From these images, it becomes clear that there is no precise 'recollimation point' – each flow line tends to hit the axis at a different point, more distant for higher initial opening angle. In both cases, the polar beam becomes rapidly unstable leading to a corkscrew with an opening angle of roughly 10°. As to the differences between these solutions, one can see that the D3D model has a somewhat larger magnetically dominated central region, especially when compared to the equatorial radius of the shock. The magnetization of this region is higher too. Finally, the shape of its termination shock resembles a bird's beak, as its radius increases rapidly after entering the narrow striped-wind zone (Fig. 14).

[2] The latter image also illustrates the grid refinement near the termination shock and at the origin.

Downloaded from http://mnras.oxfordjournals.org/ at University of Leeds on April 1, 2016

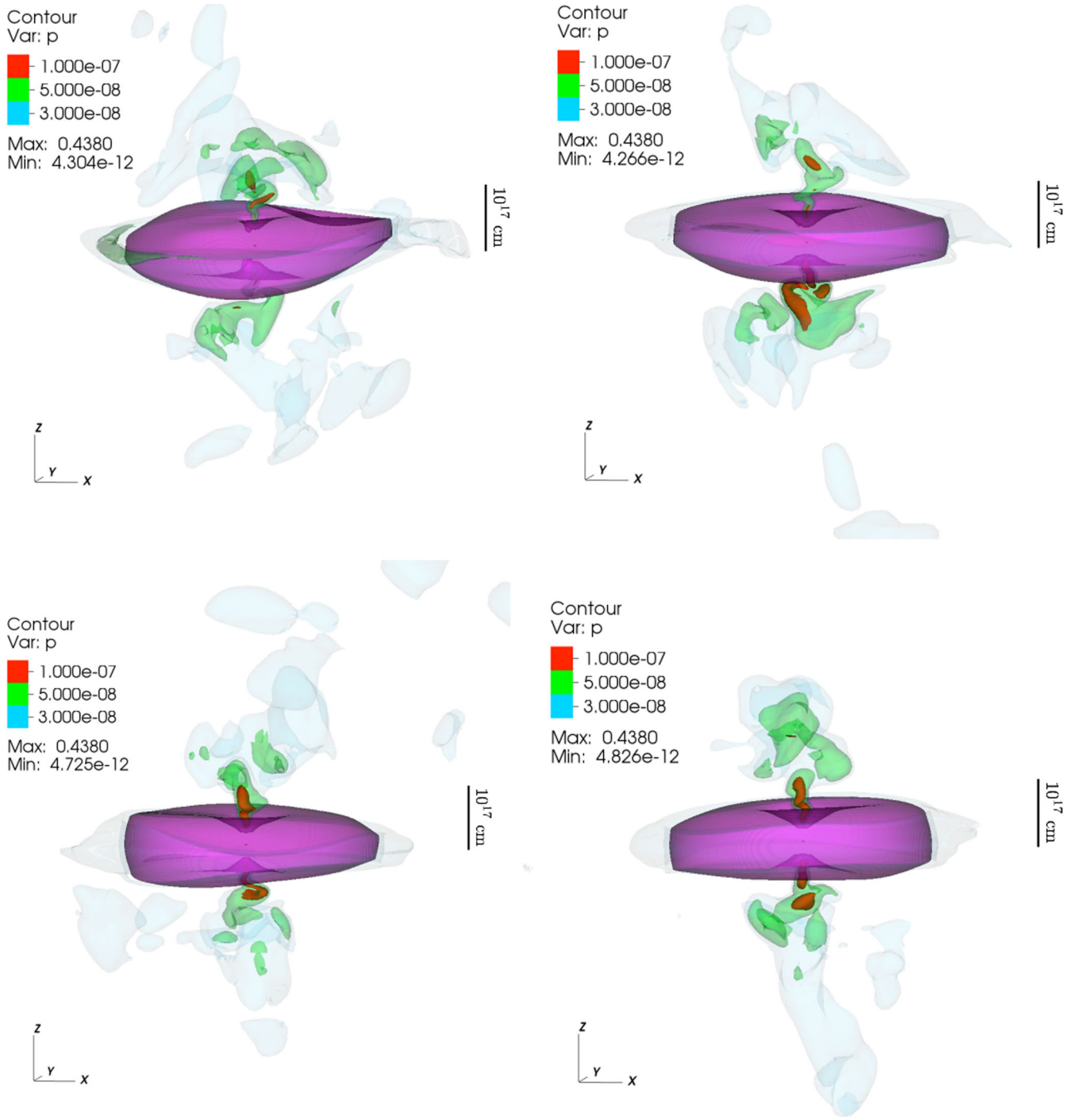

Figure 13. Termination shock and 'inner' jet. The images illustrate the simulation run B3Dhr at $t = 44$, 45, 46, 47 yr (left to right, top to bottom). The termination shock surface is shown in magenta. The inner jet region is 'illuminated' using the level surfaces of the thermal pressure. Their colour scheme is given in the plots. One can see that the polar outflow is collimated into a jet with high pressure spine already inside the 'funnel' of the termination shock. The jet exhibits corkscrew-type distortions and becomes disrupted not far from its origin. A different representation of these snapshots is shown in Fig. 6.

The plume is formed via axial collimation of the flow lines originating in the striped-wind zone. In the otherwise turbulent nebula body, this 'plume' sustains a directed flow for at least ∼6 shock radii until it eventually fragments and dissolves (see Fig. 15).

It can visually be identified in isocontours of velocity with $|u_z| = 1/3c$ surrounding a faster spine that occasionally exceeds $0.7c$. This is consistent with observations of Vela and Crab, supporting a pattern speed of 0.3–0.7c for Vela (Pavlov et al. 2003) and ∼0.4c in the case of Crab (Hester et al. 2002).

In the simulations, we observe signs of kinking and fragmentation of the plume with an overall good resemblance to the Crab jet as well.

Recently, Durant et al. (2013) showed that the Vela pulsar jet can be modelled as a helix, steadily turning on the time-scale of

Downloaded from http://mnras.oxfordjournals.org/ at University of Leeds on April 1, 2016

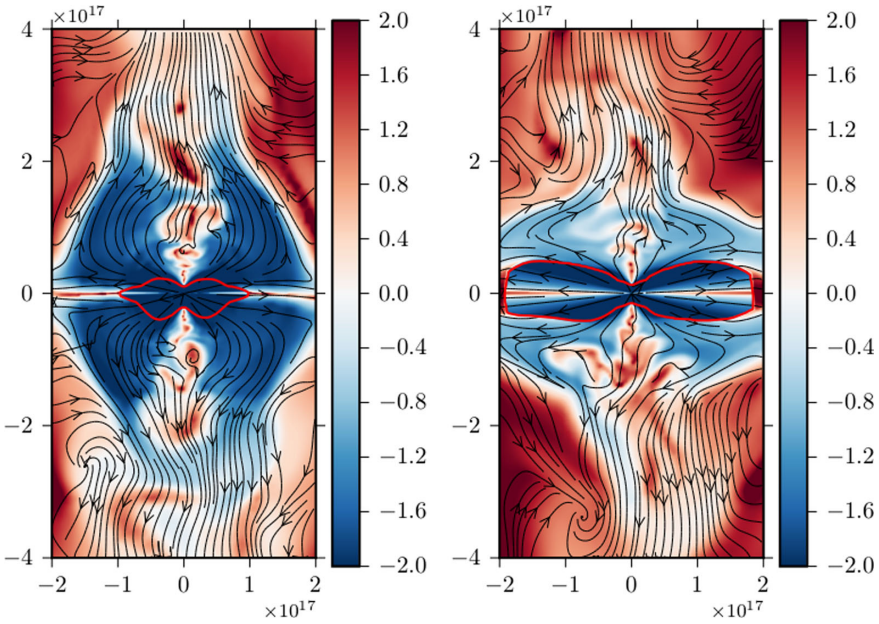

Figure 14. Formation of the polar plume. The left-hand panel shows the data for the simulation run D3D ($\alpha = 10^\circ$) and the right-hand panel for C3D ($\alpha = 45^\circ$). In both cases $\sigma_0 = 3$ and $t = 50$ yr. The colour images show the distribution of $\log_{10}\beta$ in the yz plane, the black lines the momentary streamlines and the red line the termination shock. The streamlines clearly indicate gradual collimation of the flow around the highly dissipative axial region. A coherent plume, roughly in the axial direction, is obtained after approximately one or two shock radii, depending on the obliqueness of the pulsar wind.

400 d. To this we comment that while the helical distortions due to the kink instability can be identified in individual snapshots of our simulations, we find that this structure is typically disrupted in less than a year. The helix eventually re-grows to be disrupted again shortly thereafter. The complex dynamics of the PWN makes it hard to identify a comprehensive mechanism or time-scale. This process can be observed in the second panel of Fig. 15, which shows the approaching helically deformed jet just before its disruption; two years later (last panel of Fig. 15) a new helix is formed. In the snapshot taken at $t = 48$ yr, not presented in the figure, it is dissolved again.

4 SYNTHETIC SYNCHROTRON MAPS

4.1 Particle injection prescriptions

We now compare the images obtained with different considerations for the particle injection (Section 2.2). To adopt a view similar to the Crab nebula, we choose the viewing angle measured from the pole as 60° the rotation axis thus tilts by 30° out of the plane of the sky. The assumption that the relativistic electrons and positrons are injected isotropically at the nebula termination shock (recipe A) results in the top optical image of Fig. 16. It exhibits a very bright jet-like feature, which is not present in the maps of the Crab nebula, between the pulsar and the *sprite*. The sprite itself and the opposing part of the torus are also excessively bright.

When the relativistic particles are injected only in the striped-wind section of the termination shock (the recipe B), the synthetic images are much more similar to that of the Crab nebula. The bright inner jet-like feature is absent and the emission from the sprite is significantly reduced. The sprite is produced by those streamlines of the striped wind that first converge back to the axis and thus transport emitting particles to the base of the polar plume. As to the plume itself, while this structure is certainly present in the velocity plots, it does not clearly come out in the synthetic images. 'Lighting up' the jet might require additional cycles of particle acceleration, perhaps in the unstable inner region at the base of the plume as ventured by Lyubarsky (2012).

We indicate the locations of the various features mentioned previously in the lower-left panel of Fig. 16. The right-hand panels of Fig. 16 show the synthetic X-ray images in the *Chandra* band. Due to the synchrotron burn-off, X-ray photons originate only from the torus region. Both prescriptions for particle injection give rise to the *torus* morphology, but have difficulties in reproducing the X-ray *jet* of the Crab nebula. Overall we find the prescription B more suitable and all the emission data in the rest of the paper are obtained using this prescription.

4.2 Wisps

Using the prescription B, as more suitable, we now focus on the production of concentric wisps near the termination shock in the high-resolution run B3Dhr. The motion of the azimuthal wisps can be visualized by subtracting two subsequent images, as done for example by Hester et al. (2002) using Hubble and *Chandra* imaging of the Crab nebula. Outward moving wisps are thus indicated as light arches followed by the corresponding darker features on the inside (Fig. 17). In accordance with Hester et al. (2002) and Camus et al. (2009), we space our synthetic observations by 110 d. The observed features move out with the speed of $\sim 1/3$c, roughly in agreement with the observations (Hester et al. 2002). However, likely due to the lower spatial resolution in our 3D runs compared to that of Camus et al. (2009), we can identify only two distinct wisps. Fig. 17 indicates that a fair amount of variability is also present in the sprite and shows a change in the position of the inner knot.

In the *online material*, we show a synthetic 'Hubble movie' produced from 10 snapshots taken around $t = 50$ yr and separated in time by $\Delta t = 0.1$ yr for the simulation run B3Dhr. It clearly demonstrates the outward motion of the wisps and the variability of the knot.

Downloaded from http://mnras.oxfordjournals.org/ at University of Leeds on April 1, 2016

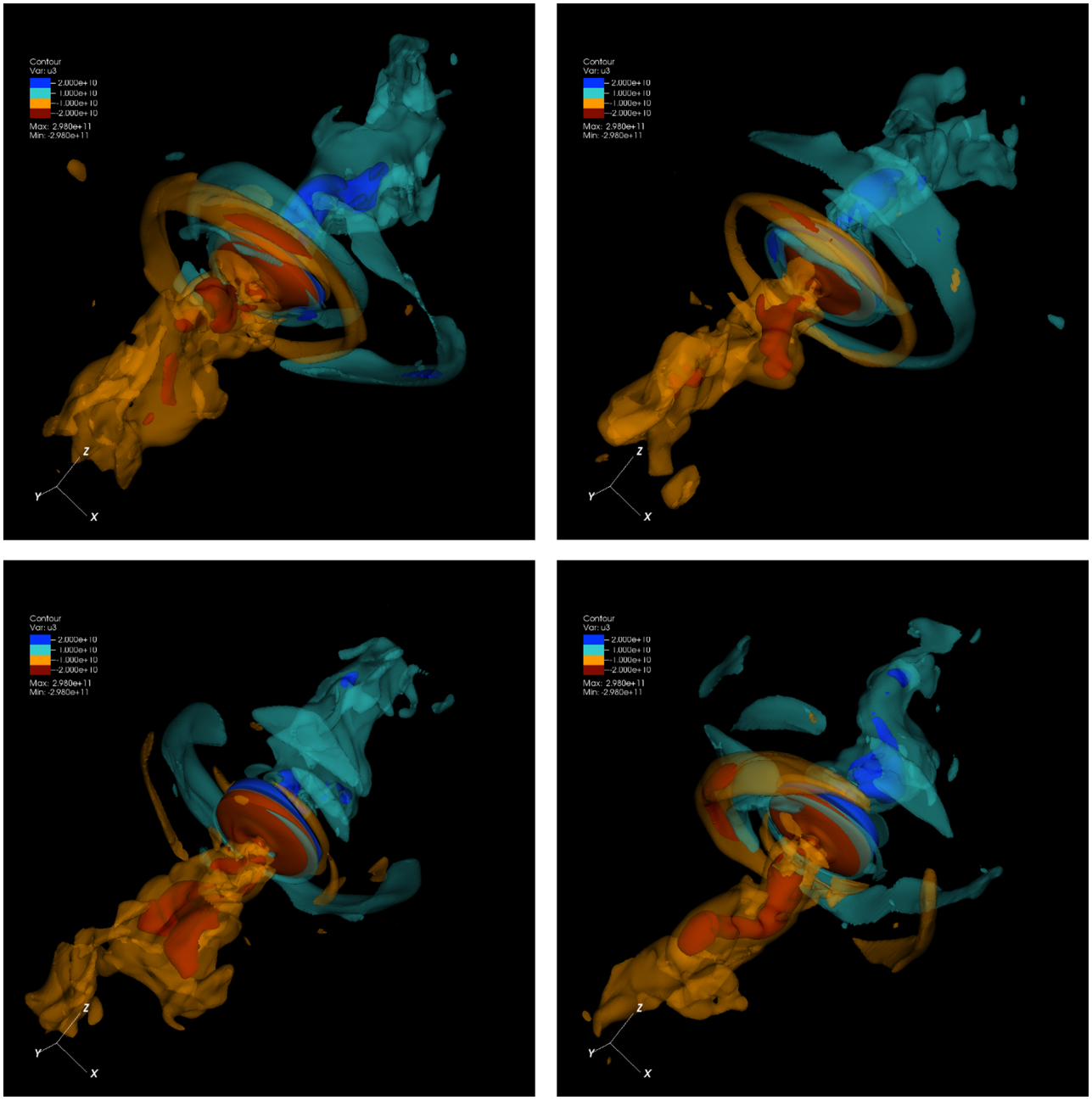

Figure 15. High-velocity flow of inner PWN. Once again we show a 3D rendering of the data for the run B3Dhr at $t = 44$, 45, 46, 47 yr (left to right, top to bottom). Now the level surfaces of u_z are used to 'illuminate' the regions of high-speed flow inside the simulated PWN. The level values are $u_z = (-2/3c, -1/3c, 1/3c, 2/3c)$. Twin jets (plumes) form downstream of the termination shock due to the 'toothpaste effect'. These jets remain coherent for several termination shock radii until they fragment and dissolve into the nebula. The right-hand panels indicate helical distortions, characteristic of the kink instability.

4.3 Inner knot

Fig. 16 shows a knot-like feature, which is located only slightly off the pulsar position in the vertical direction. In the Crab nebula, a similar knot was first discovered in the high-resolution Hubble observations by Hester et al. (1995). Its dynamical origin was explained by Komissarov & Lyubarsky (2003) as Doppler-boosted emission of the plasma just outside of the oblique section of the termination shock. The knot is an especially interesting feature of the PWN as it might be the origin of most of the gamma-rays observed from the Crab nebula (Komissarov & Lyutikov 2011). Moran et al. (2013) showed that while the intensity of the knot may vary significantly with time, the optical polarization signal remains remarkably stable and high (with a degree of 0.59 ± 0.019).

We now focus on the variability of the knot in the synthetic 'Hubble movie' data set. Thus, we zoom into the central region where the flux is dominated by the emission from this bright feature. Fig. 18 illustrates the variability of knot's shape, position and flux over the period of one year. The time-scale of the variability is around one month. For the knot flux, the standard deviation is about 10 per cent but between 50.3 and 50.8 yr it increases systematically by 35 per cent. This is comparable to the ∼40 per cent brightening over a period of two months of the Crab's inner knot reported recently by Moran et al. (2013).

Downloaded from http://mnras.oxfordjournals.org/ at University of Leeds on April 1, 2016

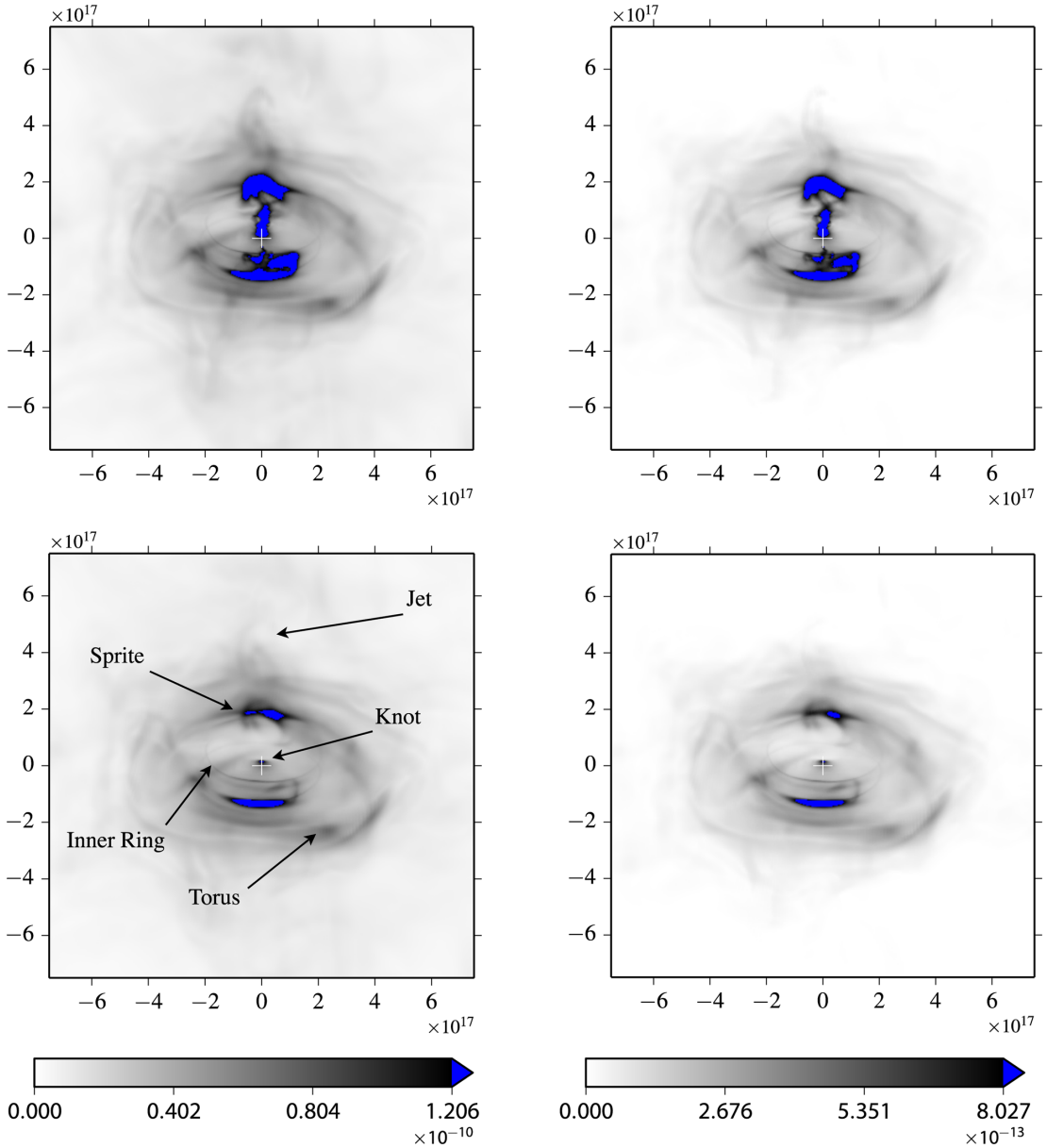

Figure 16. Optical and X-ray synthetic synchrotron images of inner PWN. The images are produced for the simulation run B3Dhr. Left-hand panels show the optical images ($\nu = 10^{15}$ Hz) and the right-hand panels show the X-ray images ($h\nu = 1$ keV). The top panels show the results based on the recipe A for the injection of relativistic particles and the bottom panels show the results based on the recipe B. In all these plots the brightness is shown using a linear scale up to 1/10 of the maximum intensity of both recipes. The location of the pulsar is marked with white '+' and saturated pixels are indicated in blue. The recipe A gives rise to excessively bright sprite and inner jet. No clear polar plume is seen in any of these maps.

The latter authors also report a relation between the knot flux and its position. To investigate the knot position in detail, we calculate the distance Δr between the intensity peak and the pulsar location in the plane of the sky. The middle panel of Fig. 18 shows the knot flux as a function of Δr. The figure indicates an anticorrelation for which we obtain the Pearson correlation coefficient between Δr and F_ν of -0.81. Thus, as the knot approaches the pulsar, its optical flux tends to increase – in good agreement to the findings of Moran et al. (2013).

The bottom panels of Fig. 18 show the degree of polarization and the electric vector position angle (EVPA) of the synthetic knot emission as measured from the projected jet axis in the anticlockwise direction. One can see that the knot polarization remains nearly constant. Within the error, the polarization degree, 0.58 ± 0.01, agrees with the early off-pulse polarization observations by Jones, Smith & Wallace (1981), Smith et al. (1988) and particularly the recent Hubble data curated by Moran et al. (2013), who separated the pulsar and knot contributions. The EVPA angle varies between $-4.^\circ5$ and $-1.^\circ5$ and thus it is closely aligned with the rotational axis of the pulsar. Such a weak variability agrees with the observations of the Crab's inner knot (Moran et al. 2013).

4.4 Nebula polarization

We have already discussed the polarization of the knot 1 in Section 4.3. Here we describe the polarization properties of the rest of the simulated nebulae. The polarization of the total flux of the Crab nebula in radio band is $\Pi = 8.8 \pm 0.2$ per cent with

Downloaded from http://mnras.oxfordjournals.org/ at University of Leeds on April 1, 2016

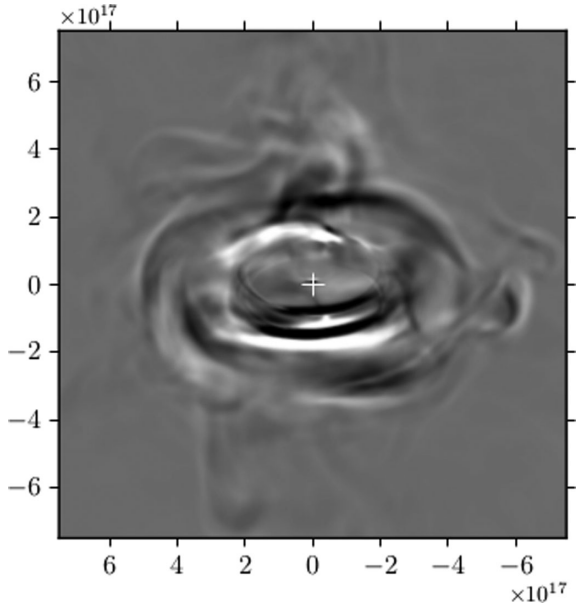

Figure 17. Moving wisps. The plot shows the difference between two optical images separated by ∼110 d, thus highlighting the variability of the emission of the inner PWN. In particular, the plot shows that the wisps move outwards (with an apparent velocity of $\sim 1/3c$). One can also see that the inner knot has shifted slightly away from the origin. A fair amount of variability is also seen in the sprite.

EVPA $\chi = 149.^{\circ}9 \pm 0.^{\circ}2$ (90 GHz; Aumont et al. 2010), in optics $\Pi = 9.3 \pm 0.3$ per cent with $\chi = 160.^{\circ}0 \pm 0.^{\circ}8$ (Oort & Walraven 1956) and in X-rays $\Pi = 19.5 \pm 2.8$ per cent with $\chi = 152.^{\circ}6 \pm 4.^{\circ}0$ (5.2 keV; Weisskopf et al. 1978). These measured EVPAs are very close to the position angle of the Crab torus symmetry axis, $\chi \simeq 126^{\circ}$ (Ng & Romani 2004) and presumably reflect the orientation of the magnetic loops injected into the nebula by the pulsar wind. The higher degree of polarization in X-ray is naturally explained as a result of the synchrotron burn-off. Indeed, because of the burn-off the X-ray emission originates from the inner region of the Crab nebula where the randomization of the magnetic field is not as strong as in the rest of the nebula volume. For optical- and radio-emitting electrons the burn-off time is much longer and as the result all parts of the PWN contribute to the integrated flux. The Faraday depolarization at 90 GHz is very small (Bietenholz & Kronberg 1991) and this explains the similarity of the radio and optical data.

From our 3D simulations we find $\Pi = 45 \pm 1$ per cent and $\chi = -0.^{\circ}79 \pm 1.^{\circ}07$ (where $\chi = 0$ corresponds to the symmetry axis) at 1 keV and $\Pi = 34 \pm 1$ per cent and $\chi = -2.^{\circ}60 \pm 0.^{\circ}83$ in the optical band. While we also find the X-ray polarization stronger than the optical one, the polarization degrees based on the simulation are significantly above the values found for the Crab nebula. The difference could be due to the shortness of the 3D runs. For example, this does not leave sufficient time for developing dense filaments via the Rayleigh–Taylor instability. The dynamic interaction of the PWN flow with the filaments is likely to enhance randomization of the magnetic field. Another possibility is an excessive magnetic dissipation in the simulations, resulting in smaller contributions to the total flux from the outer regions of the nebula where the magnetic field is less ordered.

We now discuss in detail the polarization features of our synthetic synchrotron maps for the jet–torus region. Fig. 19 shows the optical intensity maps with overlying photon *b*-field vectors, which are scaled according to the polarization degree. For comparison, we include maps based on our 2D simulations as well. In 2D, the predominant polarization *e*-field direction is that of the projected symmetry axis (see the top panels of Fig. 19), the symmetry dictating exact alignment on the polar axis. Away from the axis, the *b*-field vectors tend to curve around, tracing the azimuthal magnetic field. However, along the bright inner ring, the polarization vectors do not trace the magnetic field. This is due to the relativistic effect of polarization swing (see equation 36), which is strong because the flow velocity just after the termination shock is still quite close to the speed of light. The polarization degree is highest in the jet and in the ring. Del Zanna et al. (2006) obtained similar results based on their 2D simulations.

In 3D, the correspondence between individual features in the intensity and polarization degree maps is even more striking (the bottom panels of Fig. 19). In particular, the inner and individual wisps are clearly identified in both of them. Along the wisps, the polarization *b*-vectors are generally aligned with them. The polarization degree is close to the theoretical maximum in the forward wisps and in the knot. Not only fine features but also quite extended regions can have high polarization. For example, large patches of high polarization are seen near all four corners of the polarization degree map of Fig. 19.

According to Hester (2008) the derived magnetic field in the torus region is aligned with wisps, like in our maps, but only after subtraction of the background contribution to the polarization maps (see his Fig. 6), what we did not do. This difference may again indicate somewhat suppressed emission from the outside of the torus in our results. Hester (2008) also claims very high polarization of the wisp emission, close to $\Pi = 70$ per cent in some cases, which is in agreement of the very high polarization of the bright wisps in our synthetic maps. In more recent paper, Moran et al. (2013) give more moderate, but still high estimates $\Pi \sim 40$ per cent for the wisps. The outcome is apparently sensitive to the background subtraction algorithm. They also find that EVPA of the wisp emission is approximately aligned with the torus axis.

The reader is once more directed to the *online material* for an animation of the time series of the nebula polarization.

5 DISCUSSION

Our simulations show that a number of flow features discovered in the earlier 2D RMHD simulations of PWN are preserved in 3D. First of all, in the vicinity of the termination shock the flow of freshly injected plasma still separates into the equatorial outflow, which gives rise to the Crab torus, and the polar outflow, which is identified with the Crab jet. This was expected as the separation is due to the anisotropy of the pulsar wind power distribution and the hoop stress of the azimuthal magnetic supplied by this wind. Both these factors are inherent to the PWN models and they are introduced in the 2D and 3D simulations via identical inner boundary conditions, describing the pulsar wind. Although in 3D the azimuthal field is disrupted, this takes time and in the vicinity of the termination shock, where the separation occurs, the disruption is minimal.

In the equatorial region close to the nebula boundary, we find that the poloidal field direction can dominate over the azimuthal one. In this region, however, the average field strength is 10 times less than the field close to the termination shock. This large range of magnetic field strength calls into question the validity of 'one-zone' spectral modelling of the Crab.

Secondly, the termination shock remains unsteady in 3D, and its unsteady dynamics still yields highly inhomogeneous outflow from the shock. In the synthetic synchrotron maps, this outflow

Downloaded from http://mnras.oxfordjournals.org/ at University of Leeds on April 1, 2016

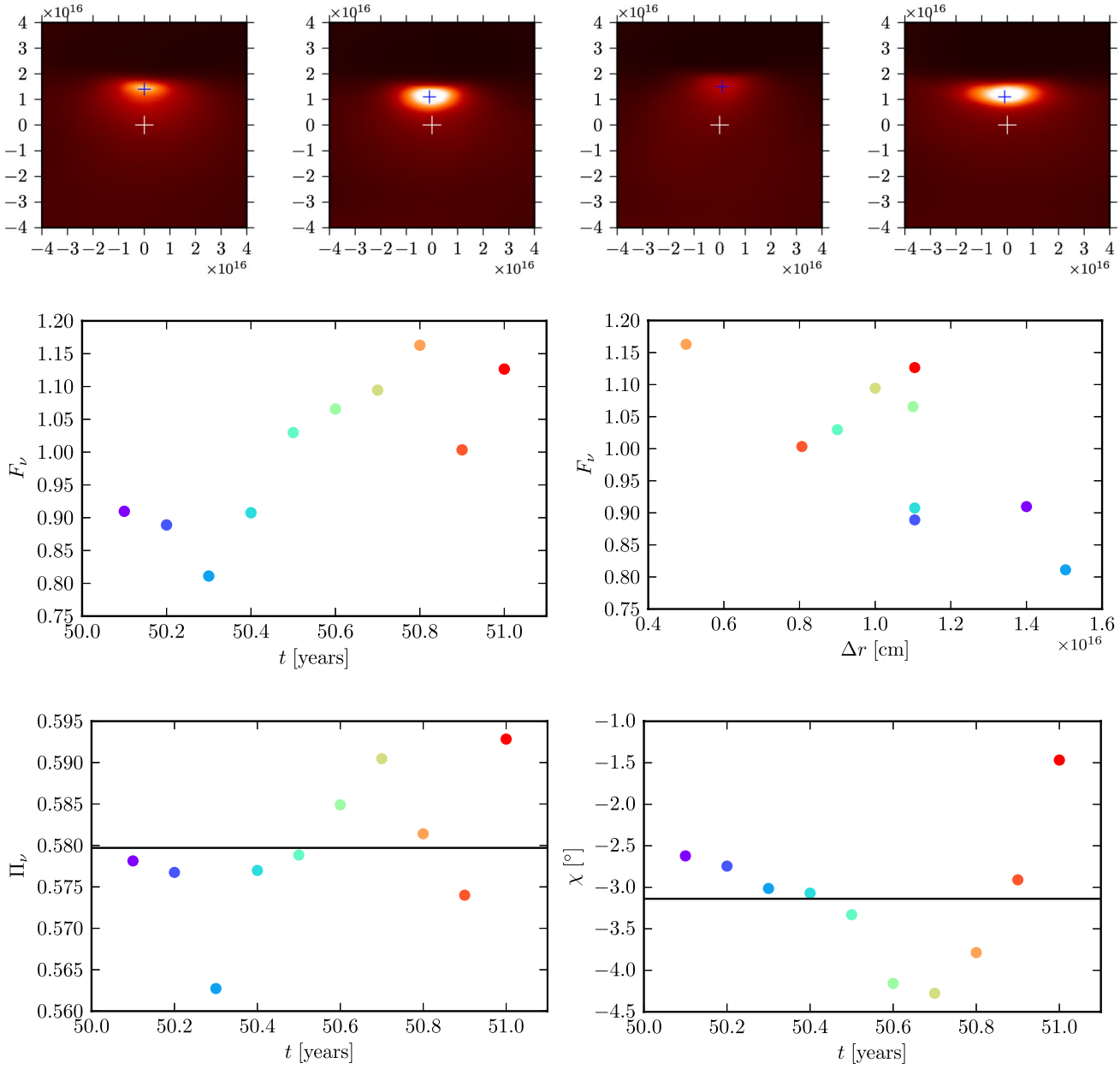

Figure 18. Variability of the inner knot. The top row shows the optical brightness distribution (linear scale) of the knot in the simulation B3Dhr for the consecutive times $t = \{50.1, 50.2, 50.3, 50.4\}$ yr. In this run, the numerical resolution at the shock is 1.1×10^{15} cm, allowing close zooming-in. As before, the position of the pulsar is marked by a white cross and we indicate the location of the intensity peak with a smaller blue cross. In the middle-left panel, we show the corresponding total flux of the knot emission (normalized to the temporal mean value) against the time and in the middle right it is shown against the separation Δr between the pulsar and the intensity peak. The data points on the panels are identified by their colour. Over the considered time span, the knot flux F_ν exhibits variability with the standard deviation of 11 per cent. The flux is anticorrelated with the separation and with the Pearson correlation coefficient of -0.81. The lower panel shows the unresolved polarization degree and the EVPA of the knot emission. These display only very weak variability. The (temporal) mean polarization degree is 0.58 ± 0.01 and the mean polarization angle is $-3\overset{\circ}{.}1 \pm 0\overset{\circ}{.}8$. Thus, the electric vector is in close alignment with the symmetry axis of the wind (the reported errors give the standard deviation). The horizontal lines just show the mean values.

appears as a collection of wisps emitted from the shock location, in a qualitative agreement with the observations of the Crab nebula. This unsteady dynamics is less violent compared to that reported in the 2D simulations of Camus et al. (2009), and the wisps are produced less frequently. This may originate in the significantly lower resolution of our simulations in the vicinity of the termination shock, leading to higher numerical viscosity and diffusion, which normally result in erasing small-scale features and may damp the shock oscillations. On the other hand, the enhanced coherency of the flow in 2D may lead to artificial strengthening of the impact which the motions in the simulated PWN make on the shape of the termination shock. In addition, we find that perturbations of the termination shock may also be triggered by non-axisymmetric instability of the polar jet.

However, our simulations have also demonstrated that the additional degree of freedom introduced in 3D models of PWN has a

Downloaded from http://mnras.oxfordjournals.org/ at University of Leeds on April 1, 2016

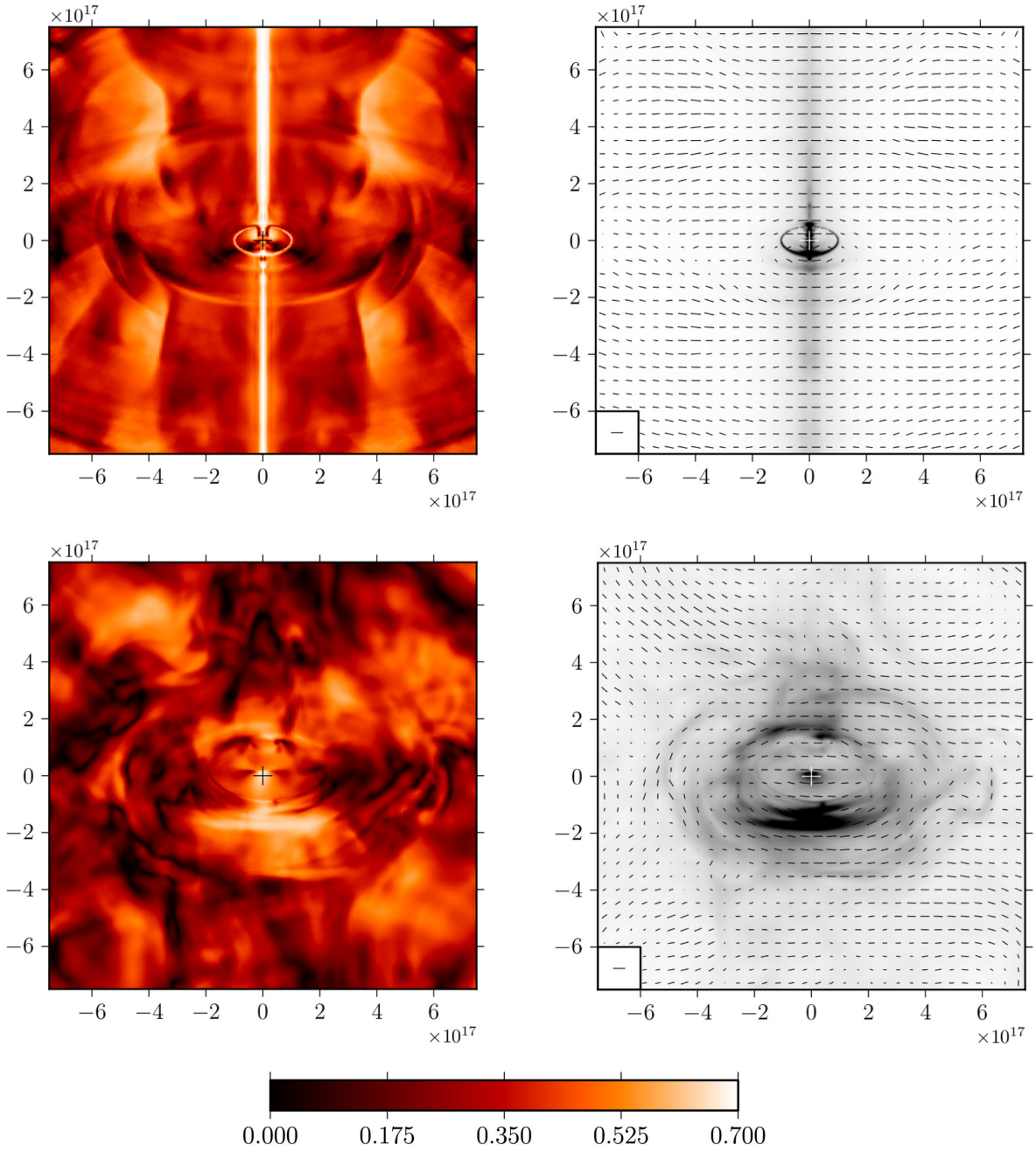

Figure 19. Synthetic optical polarization maps of inner PWN. The top panels show the maps based on the 2D simulation run B2Dhr and the bottom panels the maps based on the 3D run B3Dhr, both at $t = 51$ yr. In the left-hand panels, the colour images show the degree of polarization. In the right-hand panels, the grey-scale images show the optical intensity (linear scale) and the bars show the polarization vectors. The vectors are normalized to the maximum polarization degree of $(p + 1)/(p + 7/3) \simeq 0.7$ (indicated in the inset). Both the inner knot and the wisps are highly polarized with polarization degree close to its theoretical maximum.

strong effect on their global dynamics. The disruption of the z-pinch configuration of the axisymmetric models of PWN in our 3D simulations results in the almost complete disappearance of the strong axial compression observed in the previous 2D numerical simulations. It is preserved only above the polar section of the termination shock, the region where the polar jets (plumes) are produced. This is in agreement with Mizuno et al. (2011) who found a fast transition to the non-linear phase of the kink instability. In the plane of the sky, the Crab nebula is noticeably more extended in the direction of its jet compared to the direction of the main axis of its 'torus'. Begelman & Li (1992) explained this as a consequence of the magnetic z-pinch. In our 3D simulations, the nebula does not show such an elongation but remains very much spherical. One possible explanation for this could be an excessive magnetic dissipation – stronger magnetic field would produce stronger z-pinch. However, the calculations of Begelman & Li (1992) show that in order to achieve the observed elongation of Crab nebula in this model the magnetic pressure should be of the order of the thermal pressure, which seems to be in disagreement with the subequipartition magnetic field derived from the observations (Horns & Aharonian 2004; Meyer et al. 2010). Alternatively, the observed elongation of the Crab nebula may have nothing to do with the z-pinch but rather

Downloaded from http://mnras.oxfordjournals.org/ at University of Leeds on April 1, 2016

with the non-spherical geometry of the supernova ejecta. This could be a result of non-spherical supernova explosion (e.g. Moiseenko, Bisnovatyi-Kogan & Ardeljan 2006; Burrows et al. 2007).

In the high-σ models, we find a truly dramatic difference between the global evolutions of PWN in 2D and 3D simulations. Thanks to the artificially preserved z-pinch configuration of the 2D models, they develop extremely strong polar jets, which burst through the supernova shell. In contrast, in the 3D models the polar outflows are less powerful and eventually lose collimation and coherency via the kink instability. This difference shows that one has to be very careful and not to give too much credit to the results of 2D RMHD simulations of the jet production. In particular, our 2D jets are very similar, as well as the whole setup with purely azimuthal field, to the jets developed in the 2D simulations of the magnetar jets by Bucciantini et al. (2007, 2008), which are most likely artefacts too.

Mignone et al. (2013) studied the 3D dynamics of relativistic jets injected into an expanding cavity, with application to the Crab jet. They concluded that the observations are best fitted by the models with comparatively low jet Lorentz factors ($\Gamma \approx 2$), which is not far from we find in our simulations. However, their setup is somewhat less suitable to the Crab nebula, with the termination shock, equatorial outflow and self-consistent jet production not being incorporated. The jet instability is triggered as a result of its interaction with the strong backflow, which develops when this jet hits and 'erodes' the supernova shell. Such a strong backflow does not develop in our simulations.

The dynamics of our 3D numerical solutions shows that the magnetization of pulsar winds does not have to be as low as in the Kennel–Coroniti 1D model in order to agree with the observations. In fact, we find that even with the wind magnetization as high as $\sigma_0 = 3$, the size of the termination shock is still very close to the one predicted by an unmagnetized wind model.[3] Overall, our results provide strong support to the anticipation of Begelman (1998) that the dynamics of 3D MHD models of PWN will differ from that of 1D models in a way that can solve the σ problem. The main reason behind this anticipation was the randomization of magnetic field at the non-linear stages of the magnetic kink mode instabilities. Although the magnetic field does indeed become highly randomized, another related factor also comes into play and makes a strong impact – the magnetic dissipation inside the nebula.

Due to the magnetic dissipation in the striped wind and in the nebula, the energetics of the simulated PWN is dominated by thermal energy. Inside the nebula, the magnetic energy dissipation proceeds via two routes. First, it is the annihilation of opposing magnetic flux tubes that are blown into the nebula from the two hemispheres of the pulsar wind. The flux annihilation is amplified by the turbulence in the nebula which causes efficient mixing of the opposing polarities and transports magnetic energy to smaller scales via the turbulent cascade. Our high-resolution run indicates the emergence of an inertial range in the magnetic energy spectrum with the power-law slope of $-5/3$. Secondly, in the polar region, current sheets are produced via the kink instability of the beam and plume.

The rate of this dissipation in our simulations was high enough to result in the magnetic energy making only a small contribution to the total energy budget of the nebula. This made the composition of PWN similar to what is expected in the 1D Kennel–Coroniti model, which has no magnetic dissipation, in the case of particle-dominated pulsar wind. Unexpectedly, even our 2D numerical models had enough magnetic dissipation to not differ too much from the 3D models. In the 2D models, the dissipation is not related to the development of the magnetic kink instability. However, the current sheets are still produced by the turbulent motion in the bulk of the nebula. We conclude, that the combination of magnetic dissipation in the striped-wind zone and inside the nebula can already provide solution to the σ problem of PWN. Note that the spectral modelling of the Crab nebula suggests that its synchrotron-emitting plasma is particle dominated, thus supporting the magnetic dissipation in the nebula (Komissarov 2013).

Although the integrated equations do not have terms describing magnetic dissipation and hence all the dissipation is of numerical origin, this does not mean that it should not be taken seriously. The processes that create small-scale current sheets in our simulations and hence drive the magnetic energy flow from large to small scales, where it dissipates, are properly accommodated in the code. On the other hand, a rather high resolution is required in order to resolve even the large wavelengths of the cascade. The statistical analysis of our numerical solutions seem to indicate that the inertial range of magnetic turbulent spectrum is beginning to emerge in our highest resolution 3D simulations (see Appendix C). The convergence study, though not entirely complete, also indicates convergence of our 3D solutions in the statistical sense (see Appendix B). However, further studies are required in order to settle the matter and at this stage we cannot rule out that the rate of magnetic dissipation in our simulations is still excessive. In fact, comparing the ratio of magnetic energy to the energy in relativistic particles obtained from simplified 'one-zone' spectral models of the Crab nebula[4] with the ratio of magnetic to thermal energy in our simulations, we see that our value is lower by a factor of $\simeq 3$. On the other hand, our simulations also show that the magnetic field strength is much higher in the inner part of the nebula, where most of the Crab nebula X-ray and probably gamma-ray synchrotron emission is produced, compared to its outskirts, where most of the inverse-Compton emission is coming from. This raises doubts about the reliability of the one-zone model estimates. What is even more worrying is that the spectrum of the Crab nebula can be fitted rather well even with the 1D Kennel–Coroniti model (Meyer et al. 2010), which does not capture the PWN flow kinematics and predicts a completely different distribution of magnetic field, with the magnetic field increasing outwards. Thus, the spectral data alone does not appear to be very informative.

Given the similarities between the observed properties and theoretical models of PWN and other astrophysical phenomena involving relativistic flows, such as active galactic nuclei and GRB jets, the kink instability and magnetic dissipation can play equally important roles in their dynamics as well. In particular, this has been discussed in relation to the initial dynamics of magnetic bubbles in the magnetic model of long GRBs in Lyutikov & Blandford (2003). They speculated that while the expansion speed of the bubble is still below $0.1c$ most of the magnetic energy supplied by the central engine is converted into heat, thus producing a fireball. The results of our simulations are in full agreement with this hypothesis.

In order to provide more direct tests against the observations, we also attempted to model the synchrotron emission of the Crab nebula. In this modelling, we followed the assumption of Kennel & Coroniti (1984b) that the synchrotron electrons and positrons are accelerated only at the termination shock. However, given the recent developments in the theory of particle acceleration at relativistic magnetized shocks, we considered two cases, one where the

[3] We could not consider higher values of σ_0 because of the limitations of our numerical code.

[4] See the calculations in Komissarov (2013) and references Meyer et al. (2010), Horns & Aharonian (2004) and Hillas (1998).

Downloaded from http://mnras.oxfordjournals.org/ at University of Leeds on April 1, 2016

particles are only accelerated at the part of the shock that terminates the striped-wind zone and another where we make no distinction between the striped and unstriped zone. In both cases, the synthetic synchrotron maps reproduce the torus, inner ring, wisps and sprite of the inner Crab nebula. Moreover, the visual comparison with the Hubble images of the Crab nebula favours particle injection in the striped region only; otherwise a polar column of excessively strong emission is generated within the inner ring, in conflict with the observations. However, our simple treatment of relativistic particles produces an underluminous X-ray jet, as particles injected at the termination shock have cooled considerably until entering the plume. We suggest that additional particle acceleration in the jet is necessary to reconcile MHD models with the *Chandra* observations of the jet (e.g. Weisskopf et al. 2000). Variability of the termination shock is connected to the generation of wisps of increased intensity, moving outwards with approximate velocity of $1/3c$. This is very similar to what is seen in the *HST* observations of the Crab.[5] In our 3D simulations, the wisps maintain their arc-like shape in the torus region but become distorted further out.

The synthetic total intensity maps also show the bright extended inner knot, which was discovered in the previous 2D simulations and identified with *HST* knot 1 of the Crab nebula. Thus, this feature is very robust and not specific to 2D models only. This emission comes from the immediate vicinity of the termination shock, it is highly Doppler beamed and originates in the high-speed part of the post-shock flow. We find a correlation between knot position and flux, such that brighter states correspond to a smaller offset between knot and the location of the pulsar. The observed variability of our synthetic knot is in excellent agreement with the recent optical observations of Crab's knot 1 (Moran et al. 2013). Despite the large variability of the knot flux, the optical polarization signal of the knot is very stable with a temporal mean polarization degree of 0.58 ± 0.01, again in excellent agreement with the value reported by Moran et al. (2013). Concerning the polarization direction of the knot, we report close alignment of the EVPA with the projected spin direction of the pulsar with an angle of $-3.^{\circ}1 \pm 0.^{\circ}8$, indicative of the dominating azimuthal magnetic field of the knot. The presence of this knot in the Crab images is the most direct evidence so far of the particle acceleration taking place at the termination shock of the Crab pulsar wind.

The synthetic polarization maps show that in spite of the strong disruption of the azimuthal magnetic field supplied by the pulsar in our 3D simulations, the polarization remains substantial, particularly in the inner part of the nebula. The optical polarization direction on the scale of the torus clearly indicates an azimuthal field and photon *b*-vectors appear to curve around with the torus. The photon *b*-field direction stays aligned with the wisps, even as the wisps deform further outside. Localized features in the intensity maps (wisps, knot, jet) exhibit a strong polarization degree $\gtrsim 0.5$. This shows that the jet–torus region of the Crab pulsar is dominated by the recently supplied plasma, which still keeps memory of the highly organized magnetic field of the wind.

One feature that has a rather different appearance in our synthetic synchrotron maps compared to the images of the inner Crab nebula is the inner ring.[6] In X-rays, the real inner ring is very bright, knotty, and rather symmetric, and it does not seem have a counterpart in the optical images of the nebula (Weisskopf et al. 2000; Hester et al. 2002). In the synthetic images of 3D simulations, it is relatively weak, knotless, asymmetric and looks similar both in optical light and in X-rays. Its asymmetry is due to the Doppler beaming of the emission, which produced the fast post-termination shock flow. It is hard to see what could cancel this effect in X-rays. Perhaps, here we need to go beyond the RMHD approximation in our search for answers.

The strong magnetic dissipation observed in our simulations forces us to question the very model we used to compute the synchrotron emission. Such dissipation would almost certainly have an impact on the emission, via acceleration of synchrotron-emitting electrons (and positrons) inside the nebula, whereas in our model we followed Kennel & Coroniti (1984b) and assumed that they are accelerated only at the termination shock. The fact that our synthetic X-ray images do not show such a prominent jet-like feature as the Crab's X-ray jet already suggests that an additional channel of particle acceleration is needed to explain the observations. Other indicators are the excessively high polarization of the integral synthetic flux and the excessive brightness of the optical torus compared to the rest of the nebula (not shown). The polarization is so high because of the major contribution to the computed integral flux from the inner region (torus), where the magnetic field is still very much ordered. Provided the additional particle acceleration brightens up the outer nebula, both the polarization and the brightness contrast between the inner and outer nebula in optics may be reduced. These, however, are less convincing indicators because in the 3D simulations we have not reached the phase of self-similar expansion. Moreover, the Rayleigh–Taylor (RT) filaments did not have enough time to develop and penetrate the synchrotron nebula, which would have an impact on its dynamics. This prohibits a direct comparison of our 3D models with the observations of the whole of Crab nebula. A weaker magnetic dissipation may also help to reduce the total polarization and the brightness contrast, via increasing the magnetic field and thus the emissivity in the outer parts of the synchrotron nebula. These issues will have to be investigated in future studies.

On the other hand, our current model successfully reproduces the inner structure of the Crab nebula, with the exception of its X-ray inner ring and jet. The success of the theory in the interpretation of Crab's inner knot is particularly impressive. This allows us to conclude that the shock acceleration is still an important contributor to the nebula emission. PIC simulations of shocks in striped flow also speak in favour of such acceleration (Sironi & Spitkovsky 2011b), though they do not seem to get the right spectrum.[7] The fact that our recipe B, where the acceleration occurs only in the striped part of the termination shock, provides synthetic maps which are more reminiscent of the inner Crab nebula agrees with the PIC results. All these make a strong case for particle acceleration at the Crab's termination shock.

During a year of synthetic observation, the flux variability of the whole nebula in both soft X-ray and optical bands were on the 1 per cent level, which can be described as generally consistent with the observations (Wilson-Hodge et al. 2011, and references therein).

Concerning the origin of the gamma-ray flares of the Crab nebula, our results restrict the possible location of the magnetic reconnection events that are believed to be responsible for the flares. In order to produce synchrotron photons of the energy $\epsilon_{\rm ph}$ in the magnetic field of strength B after acceleration in the electric field of strength

[5] A movie which demonstrates this behaviour is a part of the online supplementing material.

[6] None of the synthetic maps of the nebula made by other researches have managed to reproduce this feature too.

[7] In this context, we consider the layer where the magnetic stripes dissipate as a part of the shock structure and any acceleration occurring in this layer as a kind of shock acceleration.

Downloaded from http://mnras.oxfordjournals.org/ at University of Leeds on April 1, 2016

$E = \delta B$, the magnetic field strength has to be about

$$B \simeq 3 \times 10^{-3} \delta^{-2/3} \left(\frac{\epsilon_{\rm ph}}{1\,{\rm GeV}} \right)^{1/3} \left(\frac{L}{1\,{\rm ld}} \right)^{-2/3} {\rm Gauss}, \quad (55)$$

where L is the length of the 'linear accelerator' in light days. Given that the variability time-scale can be as short as few hours (Balbo et al. 2011; Buehler et al. 2012), this length is unlikely to exceed few light days and thus the magnetic field in the reconnection layer should be well in excess of the mean magnetic field strength in the nebula, which is only $\sim 0.1 \times 10^{-3}$ Gauss (Meyer et al. 2010). Fig. 11 shows that in our numerical models, $B \simeq 10^{-3}$ Gauss can be found only in the highly magnetized polar region, which is fed by the unstriped component of the polar wind. Elsewhere, including the vicinity of the equatorial current sheet, the magnetic field is significantly weaker. Thus, the polar region at the base of the Crab jet is the most likely location of the flares.

Simulations up to the current age of the Crab nebula can only be reached with our axisymmetric models. At a nebula age of 1000 yr, we find the structure at the PWN–SNR interface in the non-linear phase of the Rayleigh–Taylor instability and dense filaments of SNR material protrude into the nebula with a length of up to 1/4 nebula radii. This is in good agreement with the prominent optical filaments observed in the Crab nebula. We will present these results in a separate paper.

6 CONCLUSIONS

(i) The jet–torus morphology of the Crab nebula, reproduced in the previous 2D RMHD simulations, is a robust feature of MHD models, which reflects the anisotropic structure of pulsar winds. It is retained in our 3D simulations.

(ii) The jets are formed downstream of the termination shock where the magnetic hoop stress causes collimation of the flow lines that pass through the shock at intermediate latitudes.

(iii) 2D models exaggerate the jet power and collimation degree. This leads to artificially strong axial compression and unphysical 'jet breakouts' in models with higher wind magnetization. This result has implications for the magnetar model of GRB central engines as it questions the mechanism of jet formation.

(iv) As in the earlier 2D models, the variability of the termination shock is caused by the intricate feedback mechanism between the shock and the nebula flow. In 3D simulations, we obtain a somewhat lower amplitude of the radial shock oscillations. The inhomogeneities, formed in the post-shock flow as a result of this variability, appear as wisps in our synthetic optical images of the Crab nebula.

(v) Our results suggest that the magnetic dissipation inside PWN could be a key factor of their dynamics. Combined with the magnetic dissipation in the striped zone of the pulsar wind, it allows us to reconcile the observations of the Crab nebula with the expected high magnetization of such winds. In particular, the termination shock radius in our run with the highest wind magnetization ($\sigma_0 = 3$) is very close to that of our lowest magnetization run ($\sigma_0 = 0.01$), as well as to the prediction of the analytical model for unmagnetized wind.

(vi) The energetics of the simulated PWN is dominated by the thermal energy. This agrees with the 'one-zone' spectral modelling of the Crab nebula. However, we also obtain a significant magnetic field variation in the nebula, which questions the validity of such simplistic spectral models. Although we cannot exclude that the magnetic dissipation rate in our simulations is too high, the results of our limited convergence study suggest that it is not completely off the scale. The low magnetic field strength, found in our simulations in the outskirts of the nebula, agrees with the subequipartion values deduced from the observations.

(vii) The strong magnetic field, $B \sim 10^{-3}$ Gauss, required in the magnetic reconnection models of the Crab gamma-ray flares, can only be found at the base of the Crab jet.

(viii) Under the assumption that the synchrotron emitting particles are accelerated in the striped zone of the pulsar wind termination shock, our synthetic images reproduce the inner structure of the Crab nebula, revealed by the Hubble and *Chandra* observations, very well indeed – we obtain dynamical counterparts for its torus, inner ring, knot and sprite.

(ix) However, an additional particle acceleration, most likely inside the jet itself or at its base, is required 'to illuminate' the jet, which is not as bright as the X-ray jet of the Crab nebula. The inner X-ray ring of the nebula remains an enigma.

(x) We have analysed the variability of the synthetic inner knot and obtained excellent agreement with the recent Hubble data. In particular, within one year the luminosity of the knot increased by 35 per cent while its unresolved polarization degree remained nearly constant at the level of 0.58 ± 0.01. Moreover, our simulations reveal a correlation between the knot flux and position, with brighter states being found at the times of smaller separation between the knot and the pulsar.

(xi) The linear polarization in the torus region is indicative of the freshly injected azimuthal magnetic field. The photon *b*-field vectors generally align with wisps, even as these deform further out. The overall polarization degree of the nebula emission is significantly higher than the observed values, both in optical light and in X-rays. Given the short duration of our 3D runs, it is not clear how significant this disagreement is. If confirmed by future longer runs, this may be considered as another evidence for particle acceleration away from the termination shock. Alternatively, this could be an indication of excessive magnetic dissipation.

(xii) More work has to be done in order to clarify a number of issues raised by our simulations. In particular, it is important to run longer 3D simulations and reach the phase of approximate self-similar expansion of the nebula. This will allow more direct tests against the observations of the Crab nebula. A more advanced convergence study is needed to settle the important issue of magnetic dissipation rate inside the nebula. An additional particle acceleration inside the nebula has to be incorporated in the model of its emission.

ACKNOWLEDGEMENTS

We would like to thank our referee, Luca Del Zanna, for very useful suggestions. SSK and OP are supported by STFC under the standard grant ST/I001816/1. SSK acknowledges support by the Russian Ministry of Education and Research under the state contract 14.B37.21.0915 for Federal Target-Oriented Programme. RK acknowledges FWO-Vlaanderen, grant G.0238.12, and BOF F+ financing related to EC FP7/2007-2013 grant agreement SWIFF (no.263340) and the Interuniversity Attraction Poles Programme initiated by the Belgian Space Science Policy Office (IAP P7/08 CHARM). The simulations were carried out on the Arc-1 cluster of the University of Leeds.

REFERENCES

Abdo A. A. et al., 2011, Science, 331, 739
Amano T., Kirk J. G., 2013, ApJ, 770, 18
Arons J., 2012, Space Sci. Rev., 173, 341
Atoyan A. M., Aharonian F. A., 1996, MNRAS, 278, 525

Downloaded from http://mnras.oxfordjournals.org/ at University of Leeds on April 1, 2016

Aumont J. et al., 2010, A&A, 514, A70
Balbo M., Walter R., Ferrigno C., Bordas P., 2011, A&A, 527, L4
Begelman M. C., 1998, ApJ, 493, 291
Begelman M. C., Li Z.-Y., 1992, ApJ, 397, 187
Beresnyak A., Lazarian A., 2009, ApJ, 702, 1190
Bietenholz M. F., Kronberg P. P., 1991, ApJ, 368, 231
Blandford R. D., Königl A., 1979, ApJ, 232, 34
Bogovalov S. V., 1999, A&A, 349, 1017
Bogovalov S. V., Khangoulian D. V., 2002, MNRAS, 336, L53
Bogovalov S. V., Chechetkin V. M., Koldoba A. V., Ustyugova G. V., 2005, MNRAS, 358, 705
Bucciantini N., Blondin J. M., Del Zanna L., Amato E., 2003, A&A, 405, 617
Bucciantini N., Amato E., Bandiera R., Blondin J. M., Del Zanna L., 2004, A&A, 423, 253
Bucciantini N., Del Zanna L., Amato E., Volpi D., 2005, A&A, 443, 519
Bucciantini N., Quataert E., Arons J., Metzger B. D., Thompson T. A., 2007, MNRAS, 380, 1541
Bucciantini N., Quataert E., Arons J., Metzger B. D., Thompson T. A., 2008, MNRAS, 383, L25
Buehler R. et al., 2012, ApJ, 749, 26
Burrows A., Dessart L., Livne E., Ott C. D., Murphy J., 2007, ApJ, 664, 416
Čada M., Torrilhon M., 2009, J. Comput. Phys., 228, 4118
Camus N. F., Komissarov S. S., Bucciantini N., Hughes P. A., 2009, MNRAS, 400, 1241
Cerutti B., Uzdensky D. A., Begelman M. C., 2012, ApJ, 746, 148
Clausen-Brown E., Lyutikov M., 2012, MNRAS, 426, 1374
Coroniti F. V., 1990, ApJ, 349, 538
Del Zanna L., Amato E., Bucciantini N., 2004, A&A, 421, 1063
Del Zanna L., Volpi D., Amato E., Bucciantini N., 2006, A&A, 453, 621
Durant M., Kargaltsev O., Pavlov G. G., Kropotina J., Levenfish K., 2013, ApJ, 763, 72
Emmering R. T., Chevalier R. A., 1987, ApJ, 321, 334
Fesen R. A., Martin C. L., Shull J. M., 1992, ApJ, 399, 599
Foy J. P., 2007, PhD thesis, Arizona State University
Harding A. K., Stern J. V., Dyks J., Frackowiak M., 2008, ApJ, 680, 1378
Heinz S., Begelman M. C., 2000, ApJ, 535, 104
Hester J. J., 2008, ARA&A, 46, 127
Hester J. J. et al., 1995, ApJ, 448, 240
Hester J. J. et al., 2002, ApJ, 577, L49
Hickson P., van den Bergh S., 1990, ApJ, 365, 224
Hillas A. M., 1998, ApJ, 503, 744
Honkkila V., Janhunen P., 2007, J. Comput. Phys., 223, 643
Horns D., Aharonian F. A., 2004, in Schoenfelder V., Lichti G., Winkler C., eds, ESA Special Publ. Vol. 552, 5th INTEGRAL Workshop on the INTEGRAL Universe. ESA, Noordwijk, p. 439
Jones D. H. P., Smith F. G., Wallace P. T., 1981, MNRAS, 196, 943
Kennel C. F., Coroniti F. V., 1984a, ApJ, 283, 694
Kennel C. F., Coroniti F. V., 1984b, ApJ, 283, 710
Keppens R., Meliani Z., van Marle A., Delmont P., Vlasis A., van der Holst B., 2012, J. Chem. Phys., 231, 718
Komissarov S. S., 2012, MNRAS, 422, 326
Komissarov S. S., 2013, MNRAS, 428, 2459
Komissarov S. S., Lyubarsky Y. E., 2003, MNRAS, 344, L93
Komissarov S. S., Lyubarsky Y. E., 2004, MNRAS, 349, 779
Komissarov S. S., Lyutikov M., 2011, MNRAS, 414, 2017
Komissarov S. S., Barkov M. V., Vlahakis N., Königl A., 2007, MNRAS, 380, 51
Komissarov S. S., Vlahakis N., Königl A., Barkov M. V., 2009, MNRAS, 394, 1182
Kritsuk A. G., Ustyugov S. D., Norman M. L., Padoan P., 2009, J. Phys. Conf. Ser., 180, 012020
Lampland C. O., 1921, PASP, 33, 79
Lazarian A., Vlahos L., Kowal G., Yan H., Beresnyak A., de Gouveia Dal Pino E. M., 2012, Space Sci. Rev., 173, 557
Lemaster M. N., Stone J. M., 2009, ApJ, 691, 1092
Lyubarsky Y. E., 2002, MNRAS, 329, L34
Lyubarsky Y. E., 2003, MNRAS, 345, 153
Lyubarsky Y., 2009, ApJ, 698, 1570
Lyubarsky Y. E., 2010, MNRAS, 402, 353
Lyubarsky Y. E., 2012, MNRAS, 427, 1497
Lyubarsky Y., Kirk J. G., 2001, ApJ, 547, 437
Lyutikov M., 2010, MNRAS, 405, 1809
Lyutikov M., Blandford R., 2003, preprint (astro-ph/0312347)
Lyutikov M., Pariev V. I., Blandford R. D., 2003, ApJ, 597, 998
Meyer M., Horns D., Zechlin H.-S., 2010, A&A, 523, A2
Michel F. C., 1973, ApJ, 180, L133
Michel F. C., Scowen P. A., Dufour R. J., Hester J. J., 1991, ApJ, 368, 463
Mignone A., Striani E., Tavani M., Ferrari A., 2013, MNRAS, 436, 1102
Mizuno Y., Lyubarsky Y., Nishikawa K., Hardee P. E., 2009, ApJ, 700, 684
Mizuno Y., Lyubarsky Y., Nishikawa K.-I., Hardee P. E., 2011, ApJ, 728, 90
Moiseenko S. G., Bisnovatyi-Kogan G. S., Ardeljan N. V., 2006, MNRAS, 370, 501
Moran P., Shearer A., Mignani R., Słowikowska A., De Luca A., Gouiffès C., Laurent P., 2013, MNRAS, 433, 2564
Ng C.-Y., Romani R. W., 2004, ApJ, 601, 479
Ohira Y., 2013, ApJ, 767, L16
Oort J. H., Walraven T., 1956, Bull. Astron. Inst. Netherlands, 12, 285
Pacholczyk A. G., 1970, Radio Astrophysics. Freeman & Co., San Francisco
Pavlov G. G., Teter M. A., Kargaltsev O., Sanwal D., 2003, ApJ, 591, 1157
Porth O., Fendt C., Meliani Z., Vaidya B., 2011, ApJ, 737, 42
Porth O., Komissarov S. S., Keppens R., 2013, MNRAS, 431, L48
Powell K. G., 1994, Technical report, Approximate Riemann Solver for Magnetohydrodynamics (That Works in More Than One Dimension). University of Michigan, Ann Arbor, MI
Rees M. J., Gunn J. E., 1974, MNRAS, 167, 1
Scargle J. D., 1969, ApJ, 156, 401
Schmidt G. D., Angel J. R. P., Beaver E. A., 1979, ApJ, 227, 106
Sironi L., Spitkovsky A., 2009, ApJ, 698, 1523
Sironi L., Spitkovsky A., 2011a, ApJ, 726, 75
Sironi L., Spitkovsky A., 2011b, ApJ, 741, 39
Smith F. G., Jones D. H. P., Dick J. S. B., Pike C. D., 1988, MNRAS, 233, 305
Tavani M. et al., 2011, Science, 331, 736
Tchekhovskoy A., Narayan R., McKinney J. C., 2010, New Astron., 15, 749
Tchekhovskoy A., Spitkovsky A., Li J. G., 2012, MNRAS, 435, L1
Uritsky V. M., Pouquet A., Rosenberg D., Mininni P. D., Donovan E. F., 2010, Phys. Rev. E, 82, 056326
van der Swaluw E., Achterberg A., Gallant Y. A., Tóth G., 2001, A&A, 380, 309
Vlahakis N., 2004, ApJ, 600, 324
Vlahakis N., Königl A., 2004, ApJ, 605, 656
Volpi D., Del Zanna L., Amato E., Bucciantini N., 2008, A&A, 485, 337
Weisskopf M. C., Silver E. H., Kestenbaum H. L., Long K. S., Novick R., 1978, ApJ, 220, L117
Weisskopf M. C. et al., 2000, ApJ, 536, L81
Weisskopf M. C., 2013, Mem. Soc. Astron. Ital., 84, 582
Wilson-Hodge C. A. et al., 2011, ApJ, 727, L40
Zhdankin V., Uzdensky D. A., Perez J. C., Boldyrev S., 2013, ApJ, 771, 124
Zrake J., MacFadyen A. I., 2012, ApJ, 744, 32

APPENDIX A: SHAPE OF THE TERMINATION SHOCK

The solution for the oblique shock is given in Komissarov & Lyutikov (2011). We utilize their (A12) for $\sigma_1 = a_1 = 0$, $\Gamma_1 \gg 1$, $\delta_1 \gg 1/\Gamma_1$ and adopt the notation of the latter authors. This gives

$$\beta_{2x}/\beta_{1x} = 1/3, \tag{A1}$$

$$\Gamma_2 = \sqrt{\frac{9}{8}}\frac{1}{\sin\delta_1}. \tag{A2}$$

The normal component of the momentum equation reads

$$\rho_1 c^2 \Gamma_1^2 \sin\delta_1^2 = p_2(4\Gamma_2^2\beta_{x2}^2 + 1) \tag{A3}$$

Downloaded from http://mnras.oxfordjournals.org/ at University of Leeds on April 1, 2016

and after substitution

$$p_2 = \frac{2}{3}\rho_1 c^2 \Gamma_1^2 \sin^2\delta_1. \tag{A4}$$

We apply these results to the pulsar wind (PW) termination shock with energy flux density profile of the wind

$$\rho c^3 \Gamma^2 \propto \sin\theta^2 \tag{A5}$$

as in the monopole solution. If p is the pressure in the nebula and L is the wind luminosity then

$$p = \frac{L}{4\pi c}\frac{\sin^2\theta}{r^2}\sin^2\delta, \tag{A6}$$

where we dropped the suffix for the obliqueness angle δ as well. Adopting $r(\theta)$ as the curve describing the shock shape, then the shock obliqueness is given by

$$\sin^2\delta = \frac{r^2}{\dot{r}^2 + r^2}. \tag{A7}$$

Introducing the length-scale

$$r_0 = \left(\frac{L}{4\pi pc}\right)^{1/2}, \tag{A8}$$

we have the dimensionless variable $\xi = r/r_0$ and equations (A6) and (A7) can be combined to

$$1 = \frac{\sin^2\theta}{\xi^2}\sin^2\delta \tag{A9}$$

whereby

$$\sin^2\delta = \frac{\xi^2}{\dot{\xi}^2 + \xi^2} \tag{A10}$$

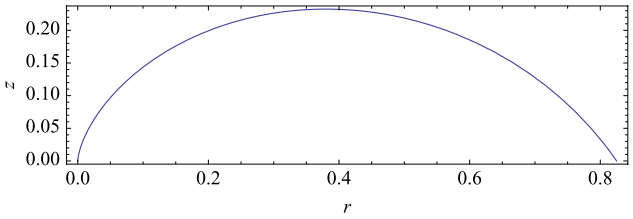

Figure A1. Numerical solution for the shock shape with $f_{\rm tot} \propto \sin^2\theta$. The unit of length is r_0.

and we end up with the non-linear differential equation describing the shape of the shock

$$\dot{\xi}^2 + \xi^2 = \sin^2\theta. \tag{A11}$$

For $\theta \ll 1$, we can make the ansatz $\xi = a\theta^b$ and obtain $b = 2$ and $a = 1/2$. Thus,

$$\xi = \frac{1}{2}\theta^2, \quad \text{for } \theta \ll 1. \tag{A12}$$

The full solution is found numerically and is presented in Fig. A1. Its properties are

$$r_{\rm max} \simeq 0.82496\, r_0 \quad \text{and} \quad z_{\rm max} \simeq 0.232462\, r_0. \tag{A13}$$

Surely, the approximation $p = $ const. is not satisfied in reality and this is why the actual termination shock is actually a complex of shocks. However, we expect the basic shock dimensions to follow this estimate which is used for the analytical reference model described in Section 2.4.

As an aside, if we assume an isotropic spherical wind, we end up with the shock radius

$$r_{\rm s} = \left(\frac{2}{3}\right)^{1/2} r_0 \simeq 0.816\,497 r_0, \tag{A14}$$

which is very close to the numerical solution for $r_{\rm max}$. Neglecting the downstream momentum we would arrive at a smaller value

$$r_{\rm s} = \frac{1}{\sqrt{3}} r_0 \simeq 0.58 r_0. \tag{A15}$$

APPENDIX B: NOTES ON CONVERGENCE

Let us now consider how the 'observables', $r_{\rm max}$ and $E_{\rm m}/E_{\rm t}$ depend on the resolution. As indicated by Fig. B1, the 3D cases show almost identical equatorial shock sizes $r_{\rm max}/r_{\rm n}$ when the resolution is doubled. We note that the 2D runs are not as well converged. Upon increasing the spatial resolution, the shock size tends to decrease as a general trend. Hence an increase of the resolution by a factor of 16 leads to a reduced shock radius and height by roughly a factor of 2 in the axisymmetric simulations. As the nebula medium is dominated by discontinuous shocks, the convergence rate is expected to be first order at best and it is not surprising that convergence of a local quantity such as the size of the termination shock is not fully reached. A likely explanation to the difference in convergence

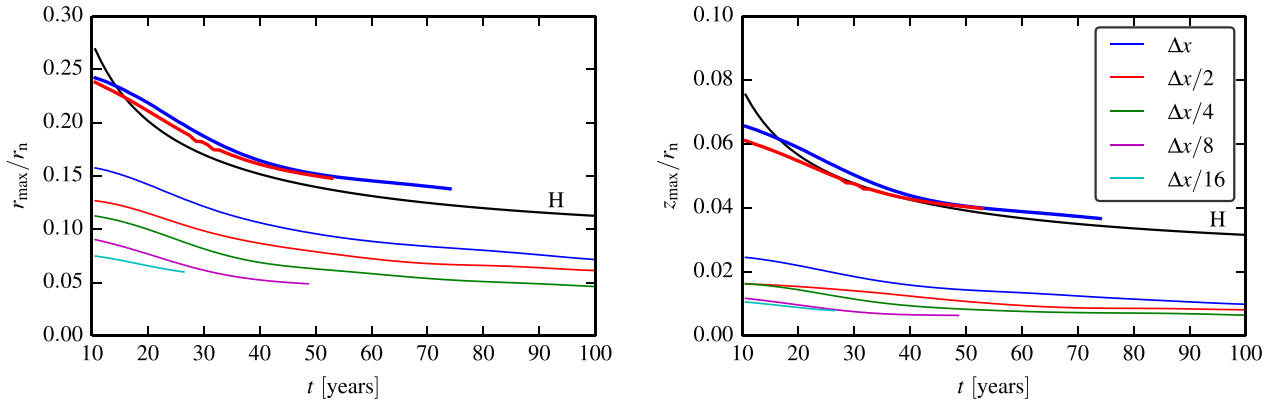

Figure B1. Maximum horizontal and vertical sizes of the TS as functions of numerical resolution. The thick and thin smooth lines show the low-pass filtered data for the 3D and 2D runs, respectively. The 3D runs seem to display well-converged shock size, whereas in 2D runs the convergence is not evident even at the resolution $\Delta x/16$.

Downloaded from http://mnras.oxfordjournals.org/ at University of Leeds on April 1, 2016

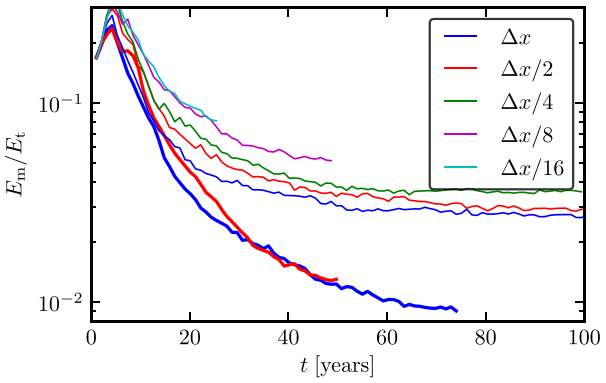

Figure B2. Magnetic dissipation as a function of numerical resolution. The plot shows E_m/E_t against the time. Like in Fig. B1, the thick lines show the 3D data and the thin lines the 2D data. The colour scheme of lines is also the same as in Fig. B1. In 2D, a convergence is noted only at the highest resolutions with $\Delta x/16$. In contrast, and in accord with our findings for the termination shock size, the 3D simulations feature early convergence again.

behaviour for the 2D and 3D cases can also be found in the presence of an artificial polar jet in axisymmetry that lacks almost entirely in 3D. The emerging strong radial gradients in azimuthal magnetic field and thermal pressure become increasingly resolved, leading to higher compression of jet and termination shock. Regardless of the lack of local convergence, our high-resolution simulations corroborate that the shock sizes are systematically underestimated in 2D, a trend that even strengthens as the resolution is increased. We stress once more that the shock radii in the 3D simulations on the other hand appear well converged.

Turning to global (integral) quantities, we show the evolution of the nebula energetics in Fig. B2. Only the highest 2D resolutions indicate convergence of E_m/E_t while the 3D realizations again show near identical evolution for Δx and $\Delta x/2$.

APPENDIX C: TURBULENT SPECTRA

Periodic boundary conditions and energy injection via 'forcing' are two elements of current direct numerical simulations of MHD turbulence [see e.g. Kritsuk et al. (2009); Beresnyak & Lazarian (2009); Lemaster & Stone (2009) or Zrake & MacFadyen (2012) for the case of RMHD turbulence]. In contrast, in the global simulations of PWN we do not use the periodic boundary conditions and do not introduce artificial force terms. The turbulence is produced via instability of the equatorial flow and polar jet as well as the unsteady termination shock, all taken into account in a self-consistent manner. The pulsar wind injects strong (azimuthal) guide field, a particularly interesting case of MHD turbulence. The turbulent flow is naturally confined by the expanding supernova shell which acts like a reflecting wall for the waves generated inside the nebula. All these render the PWN an ideal host to study RMHD turbulence.[8]

If a turbulent cascade develops in the nebula, the energy is transported from the driving scale over the self-similar inertial range to the dissipation scale, which in our case is determined by the numerical resolution. In order to properly account for the dissipation, the inertial range has to be resolved in the simulations. Since the dissipation of the magnetic energy injected by the wind plays a key role in the dynamics of the PWN, this issue gains particular importance.

To obtain magnetic and velocity power spectra, we select a subdomain containing the entire nebula with $x, y, z \in (-1.5 \times 10^{18}, 1.5 \times 10^{18})$. Inside this subdomain, the numerical solution is mapped on to a uniform grid with the same resolution as that used for the integration inside the nebula and away from the termination shock, where the resolution is higher. This corresponds to 150^3 grid cells in the fiducial case and 300^3 cells for the high-resolution case. Then we perform the 3D discrete Fourier transform

$$\hat{X}(m,n,l) = \frac{L_x}{N_x}\frac{L_y}{N_y}\frac{L_z}{N_z}\sum_{i=0}^{N_x-1}\sum_{j=0}^{N_x-1}\sum_{k=0}^{N_z-1} X(i,j,k) \tag{C1}$$

$$\exp\left[-2\pi i\left(\frac{mi}{N_x}+\frac{nj}{N_y}+\frac{lk}{N_z}\right)\right], \tag{C2}$$

where $m \in [-N_x/2, N_x/2]$, $n \in [-N_y/2, N_y/2]$ and $l \in [-N_z/2, N_z/2]$ are integers that span from the negative to the positive Nyquist frequency. The magnetic power in the (m, n, l) spatial frequency domain is defined as

$$P_m(m,n,l) = \frac{1}{8\pi}\left(\hat{\boldsymbol{B}}(m,n,l)\cdot\hat{\boldsymbol{B}}^*(m,n,l)\right), \tag{C3}$$

where the superscript * indicates the complex conjugate. Next, assuming isotropy in k-space, we average over spherical shells:

$$P_m(k) = 4\pi k^2\langle P_m(m,n,l)\rangle_S(k) = 4\pi k^2\frac{\sum_{k-\Delta k}^{k+\Delta k} P_m(m,n,l)}{\sum_{k-\Delta k}^{k+\Delta k} 1}, \tag{C4}$$

whereby the sum is taken over all elements within the shell, $k(m,n,l) = \sqrt{(m/L_x)^2+(n/L_y)^2+(l/L_z)^2} \in [k-\Delta k, k+\Delta k)$. This yields the spectral energy density normalized such that the continuous limit results in

$$\frac{1}{8\pi}\iiint B^2(x,y,z)\,\mathrm{d}x^3 = \int P_m(k)\,\mathrm{d}k \tag{C5}$$

by Parseval's theorem.

To reduce the noise in the spectra, the temporal average

$$\bar{P}_m(k) = \langle P_m(k)\rangle_t \tag{C6}$$

is performed over 11 consecutive snapshots starting at $t = 20$ yr with $\Delta t = 1$ yr.

Fig. C1 shows the shell-averaged power spectra for the 3D runs B3D and B3Dhr which differ only by their resolution (see Table 1).

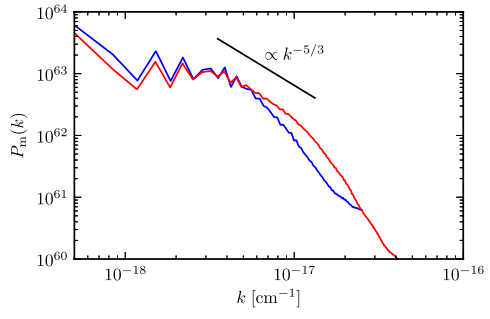

Figure C1. Shell-averaged power spectra of the nebula magnetic field in the 3D runs. The blue lines show the data for the run B3D and the red ones for the run B3Dhr which has doubled resolution. The magnetic energy spectra indicate emergence of the inertial range in the higher resolution run. In this range, the magnetic energy varies approximately $\propto k^{-5/3}$.

[8] In addition, the MHD turbulence can be responsible, at least in part, for the particle acceleration in the nebula proper via wave-particle interactions or turbulent shear acceleration (e.g. Lazarian et al. 2012; Ohira 2013).

Downloaded from http://mnras.oxfordjournals.org/ at University of Leeds on April 1, 2016

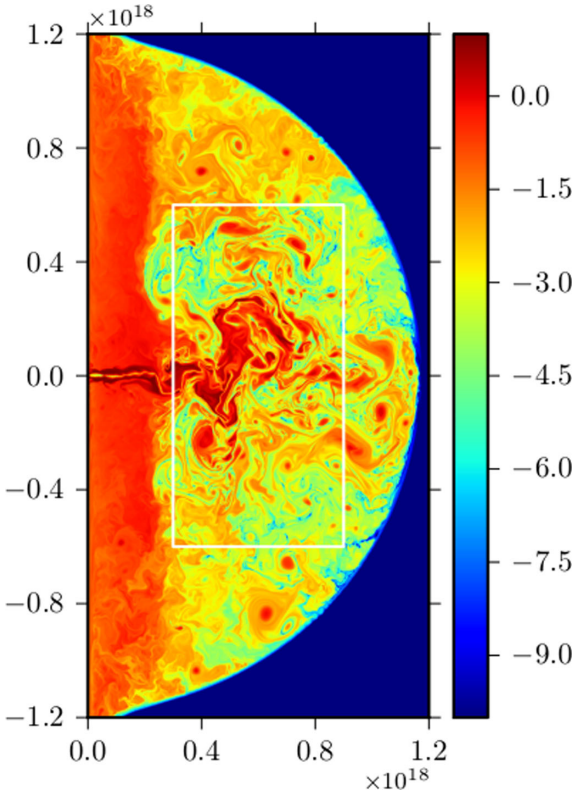

Figure D1. Box of the turbulent region at $t = 28$ yr, shown is the magnetization $\log_{10}\sigma_s$ in the highest resolution run B2Dehr.

A quick inspection of the data shows that the large-scale structure is well reproduced in the simulations. The magnetic energy spectra indicate the emergence, in the higher resolution run, of an inertial range with the spectral index $-5/3$. The corresponding power spectra for our 2D runs are described in Appendix D.

APPENDIX D: 2D POWER SPECTRA

We consider a rectangular test volume in the shocked region of the turbulent nebula bubble with $r \in (3 \times 10^{17}, 9 \times 10^{17})$ and $z \in (-6 \times 10^{17}, 6 \times 10^{17})$ cm to exclude the wind zone and the polar jet (see Fig. D1). To obtain results independent of the interpolation technique, the spectra are cut at the Nyquist frequency corresponding to the original grid spacing in the nebula part of the domain.

Power spectra in 2D (m, n) space are obtained analogue to the 3D case. In 2D, the shell average becomes

$$P_{\rm m}(k) = 2\pi k \langle P_{\rm m}(m,n)\rangle_s(k) = 2\pi k \frac{\sum_{k-\Delta k}^{k+\Delta k} P_{\rm m}(m,n)}{\sum_{k-\Delta k}^{k+\Delta k} 1}, \qquad \text{(D1)}$$

whereby the sum is taken over all elements within the shell, $k(m,n) = \sqrt{(m/L_r)^2 + (n/L_z)^2} \in [k - \Delta k, k + \Delta k)$.

Fig. D2 shows the averaged power spectra of magnetic field and four-velocity for the 2D simulations.

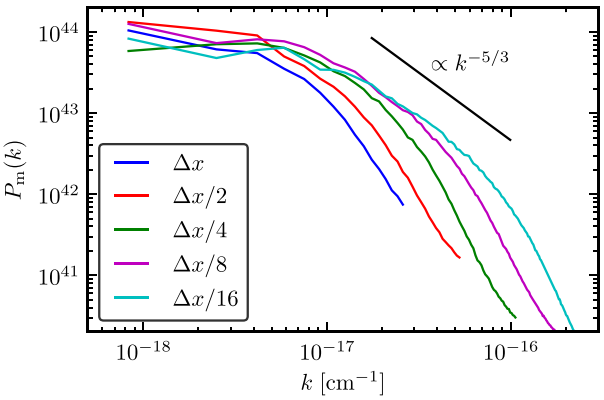

Figure D2. Shell-averaged power spectra of the magnetic field in the test volume. The magnetic power spectrum shows an approximate inertial range $\propto k^{-5/3}$. In agreement with results shown in Appendix B, no convergence is found for the 2D case leading to an increase of the area under the curve with increasing resolution.

Even with the highest resolution, the inertial range is barely resolved and indicates a scaling according to $k^{-5/3}$. This is consistent with the lack of convergence of the observables noted in the previous section.

SUPPORTING INFORMATION

Additional Supporting Information may be found in the online version of this article:

Movie 1 (45d_s1_3Dhr.avi). Optical synthetic movie of the inner PWN at $\nu = 10^{15}$ Hz. The frames are spaced 40 days apart and show emission recipe B with linear scale in simulation B3Dhr. The location of the pulsar is marked with white '+'. Within a time-span of one year, several wisps emanate from the termination shock. Spatial and intensity variations of the knot can be observed on roughly monthly timescales.
Movie 2 (45d_s1_3DhrPOL.avi). As Movie 1 (45d_s1_3Dhr.avi) with added photon b-field polarization vectors, normalized to the maximal polarization degree of 0.7 (indicated in the inset).
(http://mnras.oxfordjournals.org/lookup/suppl/doi:10.1093/mnras/stt2176/-/DC1).

Please note: Oxford University Press are not responsible for the content or functionality of any supporting materials supplied by the authors. Any queries (other than missing material) should be directed to the corresponding author for the article.

This paper has been typeset from a TEX/LATEX file prepared by the author.

Downloaded from http://mnras.oxfordjournals.org/ at University of Leeds on April 1, 2016